UiT

THE ARCTIC
UNIVERSITY
OF NORWAY

Faculty of Science and Technology
Department of Physics and Technology

On the Meteoric Smoke Particle Detector SPID:

Measurements and analysis from the G-chaser rocket campaign
—

Henriette Marie Tveitnes Trollvik
Master thesis in Space Physics, FYS-3931 - June 2019

Abstract

The Smoke Particle Impact Detector (SPID), newly designed at the University of Tromsø, was launched from Andøya 09:13 UTC the 13. January 2019. SPID is designed to detect meteoric smoke particles (MSPs) in winter mesospheric conditions. The rocket had a velocity of 1600 ms−1 at ~55 km where the nosecone was separated. At ~ 60km, SPID detected a signal of 17nA on the middle plate. The dynamics of the particles entering the detector was investigated taking into account the drag of the neutral airflow as well as the electric field generated by the bias voltages of the detector. These conditions were applied to a model of the size and charge of mesospheric dust in the range of radii 0.5 to 8 nm. For this model of the meteoric dust we find that 97 percent of particles that the rocket encounters would reach the middle plate and that 30 percent of the particles would hit the middle plate directly at 60 km. Estimations of dust densities that could explain the measured current vary between 10^{10} and 10^{13} per m^3. The density of positive ions is close to that of MSPs, and so it is also possible that the measured current, or a fraction of it, is caused by ions. A secondary goal of the campaign was to investigate the relation between MSPs and the winter radar echoes called Polar Mesospheric Winter Echoes(PMWE). For this, the background atmospheric conditions were monitored with the radar systems MAARSY (53.5 MHz) and EISCAT (224 MHz). The EISCAT measured incoherent scatter which showed weak precipitation above 85 km. MAARSY did not observe PMWE activity during the launch, but on the days prior and after launch. Because it is a prerequisite to observe PMWE that the electron density is sufficiently high, we cannot draw any conclusions on the link between PMWE and MSP from the presented observations. The spectral analysis of the measured current shows strong rotational effects at higher altitudes. The Power spectrum follows the Kolmogorov slope of $k^{-5/3}$ into the Bragg scale of MAARSY(~2.8), suggesting turbulent conditions influence the current. Because the resolution of the SPID is close to the Bragg scales of MAARSY, no clear conclusion could be made for the Bragg scale turbulence conditions.

Acknowledgements

List of Figures

List of Tables

Contents

/1

Introduction

One of the main reasons why humans can exist on Earth is due to the atmosphere and the magnetic field. Together they provide a shield from radiation and incoming energetic particles, like the solar storms. The atmosphere stretches from the ground all the way out to around 1000 km. Its upper part from about 60 to 1000 km is ionized by solar radiation, called the ionosphere. The lower ionosphere overlaps with the upper mesosphere. The mesosphere is characteristic in that it has a decreasing temperature gradient, reaching the minimum temperature in a region referred to as the mesopause. The mesosphere (at roughly 50 to 90 km) displays several physical phenomena, and some of them involve solid dust and ice particles.

Every day the earth is bombarded with meteoroids, on the order of 10-100 metric tons. The meteoroids entering Earth's atmosphere collide with atmospheric constituents and through this process loose material. When the atmospheric density is sufficiently high, sufficiently high that meteoroids are heated to vaporization temperature, meteoroid material remains in the atmosphere. This occurs in the upper mesosphere. Some of the residues, through reactions with the constituents of the mesosphere, make up meteoric smoke particles (MSPs). These particles are of sizes 1-10 nm and are believed to be located throughout the mesosphere. MSPs act as ice nuclei for ice particles, related to polar mesospheric summer echoes (PMSE) and noctilucent clouds (NLC). The mesospheric charge balance is also affected by the presence of MSPs and charged MSPs are believed to be related to polar mesospheric winter echoes (PMWE). There is

also an indication that they are important in understanding the chemistry of the middle atmospheric (stratosphere and mesosphere), chemistry. Both the size and altitudes in which MSPs exist make them hard to observe directly. They are out of reach for balloon experiments, and too low for satellites. Ground-based radars and satellites are able to observe the mesosphere, but the observations have low altitude resolution and are inadequate for observing MSPs on the size of order 1 nm. The best method for conducting in-situ measurement in the mesosphere is to use rockets.

In 2017, a student rocket campaign, G-CHASER, was initiated as part of the Grand Challenge Initiative, aiming to investigate the north polar cusp region. G-CHASER is a student rocket, with teams from universities in Japan, Norway, Puerto Rico and the US. It was launched from Andøya, 13. January 2019 09:13 UTC. Onboard were eight student instruments, including one from the University of Tromsø (UiT), the Smoke Particle Impact Detector (SPID). SPID is a Faraday cup impact detector, with heritage from two previous detectors, MUDD and DUSTY, also developed by UiT. The main difference between SPID and the two previous detectors is that SPID is specifically aimed at detecting MSPs in polar winter mesospheric conditions, while MUDD and DUSTY were designed for summer conditions, thus detecting larger ice particles. The rocket pass the atmosphere at supersonic speeds and the motion of air into and around the probe highly affects particles of nanometer size. In designing a new probe for detection of the nm-sized particles, several theoretical considerations must be considered. These are particularly in relation to the neutral and charged particle flow. To obtain information on the background conditions during the launch the radar systems MAARSY and EISCAT were operating in addition to the instruments on the rocket. MAARSY, a VHF radar located at Andøya measured the PMWE activity in the predicted trajectory, while the EISCAT VHF and UHF in Ramfjordmoen measured the ionospheric conditions. The measurements will be used to determine the electron density and ionospheric activity at time of the launch. It will also provide helpful background information to support the measurements done by the rocket.

The goal of this thesis is to use the data obtained from SPID, in combination with information about the the field conditions and the air flow to derive the trajectories and sizes of the dust entering the instrument. The height profile of the detected dust layer will be derived, the influence of external events on the measurements will be considered. The rocket observations will be compared to radar observations of PMWE and of ionospheric conditions, like particle precipitation, to search for a possible link between PMWE occurrence and the presence of MSPs.

This thesis is structured in the following way: Chapter 2 introduces physics of the atmosphere and circulation patterns, meteoric dust and the radar phenomena of polar mesospheric winter echoes. These topics provide the background for the SPID probe, which will be the focus of this thesis. Chapter 3 describes the SPID probe, explaining the design, mechanics, testing and the detection process. The models used for analysis are presented in chapter 4. Chapter 5 presents the neutral air flow, electric field and particle trajectory simulations. Considerations regarding the ion motion and plasma conditions will also be discussed. In chapter 6 the G-chaser campaign is introduced, where all student teams are presented. It will also include details on the testing and launch conditions. Chapter 7 contains the data analysis, including effects on the current due to timer events, consideration of the background current and a spectral analysis of the signal at various height. Chapter 8 contains a conclusion.

/2

Background

In understanding the results and process of analysis related to a rocket campaign, it is essential to understand the background of the experiment. This chapter will go into detail on the physical phenomena connected to meteoric smoke particle and dust in the mesosphere. This chapter is based on review papers and textbooks.

2.1 Earths atmosphere

Earth is exposed to a range of hazardous phenomena every day. The atmosphere shields and absorbs the surface from radiation, making the earth a habitable planet. In combination with the absorption and the force balance between gravity and pressure, local temperature changes occur, resulting in stratified layers. Temperature differences and pressure differences give rise to intricate circulation patterns, mixing the atmosphere and its contents. Figure 2.1 names the different regions, where the graph indicate the temperature changes with altitude. The lowermost regions, being the troposphere and stratosphere, gives rise to the weather system. The stratosphere contains ozone which absorbs UV, resulting in a positive temperature gradient. In the next layer, the mesosphere, the temperature decrease reaching the lowest temperatures in the atmosphere. In the summer, it can drop to ~ 150K. The thermosphere is the last defined layer of the atmosphere, with increasing temperature up to $\sim 1000k$ at the thermopause, where interplanetary space begins Schunk and

Nagy (2009).
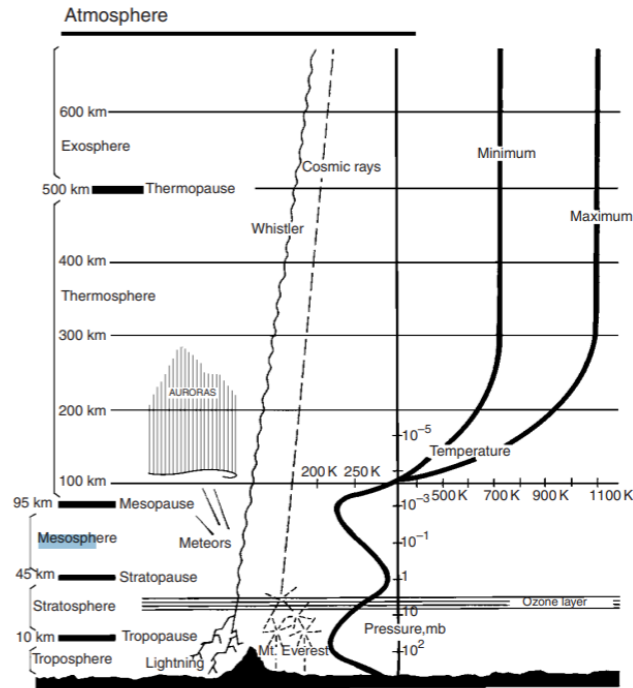
Figure 2.1: Diagram showing the different domains and phenomena in the Earth's atmosphere. The solid black lines indicate the temperature profile for solar minimum and maximum conditions, in the equatorial region. Adapted from Schunk and Nagy (2009)

The altitudes between 60 km to 1000 km is referred to as the ionosphere. Here the neutral species are ionized by extreme ultraviolet radiation from the sun and colliding energetic particles. There is a significant amount of free thermal electrons and ions, which are affected by a range of processes. These processes include chemical reactions, plasma instabilities, wave disturbances, diffusion and transport due to electric and magnetic fields. The electron density variation gives rise to a layered structure, divided into the D (60-100km), E (100-150) F_1(150-250) and F_2() regions. In this thesis, the main focus will be on the altitude range between 55 and 90km, within the mesosphere and D region.

2.1.1   The Mesosphere

The mesosphere is a very chemically active region, where both positive and negative ions exist, dominated by cluster ions formed via hydration of NO^+ and O_2^+ (Schunk and Nagy, 2009). The most abunant neutral species are N_2, O_2, and O. The rotation of the earth results in global circulation patterns in the atmosphere. The circulation causes equatorial flow in the summer pole and poleward flow in the winter pole. As a result, there is up-welling of air at the summer pole, cooling the air by adiabatic expansion. The summer mesospheric temperatures can reach down to 150 K; well below the local dew point of water. In the winter there is down-welling, transporting air from the entire global mesosphere to the winter pole. As a result, there is an inverse temperature change from summer to winter, giving rise to seasonal variations and related phenomena such as polar mesospheric winter and summer echoes (Plane et al., 2015). At mesospheric altitudes, the decrease in density is sufficient to result in unstable waves and the occurrence of turbulence (Megner, 2008).

Turbulence describes fluid motion that is highly distorted, occurring at high velocities. The motion is the result of the inertial forces are large compared to the viscous forces, i.e a large Reynolds number, and random and rapid fluctuations govern the fluid motion (Yunus, 2014). Kevin-Helmholtz shear instabilities and gravity waves breaking are the two most common mechanisms of creating turbulence in the mesosphere (Belyaev, 2019). Gravity waves are waves originating from the troposphere, where the driving force is gravity or more specifically buoyancy. These waves are generated due to density changes, which occur in wind shears, cumulonimbus cloud formation or in the presence of stratification (Vallis, 2017). Gravity waves propagate upwards in the atmosphere, transporting energy from the troposphere up to the higher regions. As the wave travels upward through the mesosphere, the decrease in temperature causes the amplitude of the wave to increase, until it becomes unstable and breaks. The wave breaking transfers kinetic energy and momentum to the mesosphere, resulting in turbulence. Another effect of the gravity waves breaking, is a drag zonal winds, causing a meriodal flow in the middle and upper mesosphere to the winter pole (Becker and Schmitz, 2002).

Fluid flows can be characterized by their wavenumber dependence, related to the dissipation rate of energy in the flow, i.e Schmidt number S_C and the flow region of the fluid, i.e Reynolds number R_e (Yunus, 2014). Kolmogorov (1941) stated that a flow should follow a $k^{-5/3}$ wavenumber dependence for large Reynolds numbers. The flow would then be in the inertial subrange of viscosity, dominated by inertial forces. For smaller Raynold numbers the flow should follow a k^{-7} wavenumber dependence, indicating a viscous subrange (Heisenberg, 1948). At these scales, molecular diffusion and viscosity dominate the flow, and irregularities practically do not exist (Rapp and Lübken, 2004).

Tracers can be used to measure the fluctuations in the neutral air turbulence. These tracers must be passive and conservative. Passive meaning that they do not influence the flow. Conservative meaning that they do not change in time, other than due to the turbulent motion (Lübken et al., 1993). Examples of such tracers are neutral density fluctuations, ion density, electron density and Meteoric Smoke Particles (MSPs), which have been measured in-situ using rocket born instruments (i.g Lübken et al. (1993); Rapp et al. (2003); Brattli et al. (2006); Spicher et al. (2014); Antonsen et al. (2019)).

2.2 Mesospheric dust

For decades the topic of meteoric dust particles has been of interest for scientists. These particles are believed to be connected to several mesospheric phenomena. They play a crucial role in the charge balance of the middle atmosphere and has a significant effect on the middle atmospheric chemistry. This section will go into summarizing the current understanding and observations of meteoric dust particles (ice and smoke), with focus on the meteoric smoke particles(MSPs).

2.2.1 Formation

A vast amount of meteoroids exist in interplanetary space. These are objects considerably smaller than asteroids, but much larger than a molecule. The exact amount of meteoric material entering the earth daily is unclear, but estimates suggest somewhere between 10-100 metric tons. Between 120 - 80 km, upper mesosphere-lower thermosphere, meteoroids have become sufficiently heated to evaporate, at which point they appear as meteors (Mann, 2009). Studies have found that the major constituents of the mesosphere originating from meteoric ablation, are Fe, Mg and Si, in similar quantities. In the presence of O_3, O_2 and H_2O, the metals oxidize, and make up species such as FeOH, $Mg(OH)_2$ and SiO_2, serving as the basic composition of meteoric vapours (Plane et al., 2015). These vapours are believed to undergo re-condensation processes ((Hunten et al., 1980); (Bardeen et al., 2008); Megner et al. (2006)) to form meteoric smoke. Coagulation and condensation forms the smoke to particles, ranging from 0.1 Å to a few nm, and traverse down in the atmosphere due to gravitational sedimentation ((Rosinski and Snow, 1961)(Saunders and Plane, 2006); (Plane et al., 2015)). The MSPs act as condensation nuclei in the summer mesosphere, where the temperature drop bellow the dew point of water.

To estimate the concentrations of the constituents of the D-region, chemistry

models can be used. One of these models is the Sodankylä Ion and Neutral Chemistry (SIC) model, including MSP processes (Baumann et al., 2015). Another model, applied to MSPs, is the Community Aerosol and Radiation Model for Atmospheres (CARMA) Megner et al. (2006). Figure 2.2 show MSP and ion distribution for September conditions, adapted from SIC model done by Baumann et al. (2015) based on the size distributions derived by Megner et al. (2006).
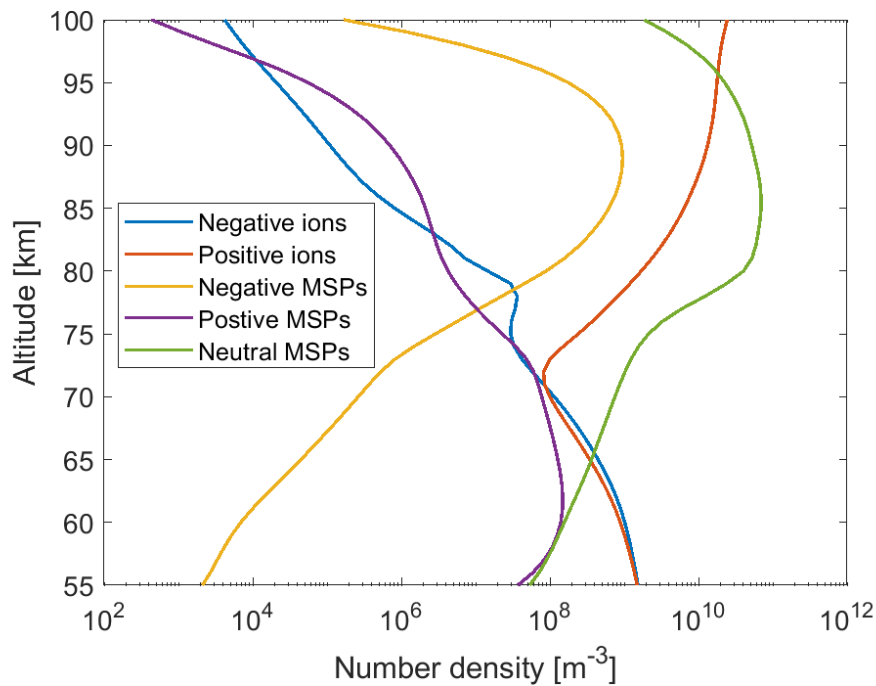
Figure 2.2: MSP and Ion distribution for september conditions. Adapted from simulations conducted by Baumann et al. (2015) with size distribution from Megner et al. (2006).

2.2.2 Related phenomena and observations

As a result of the circulation pattern, theories suggest significant seasonal variations of the MSPs distribution and height distribution (Bardeen et al., 2008)(Megner et al., 2006). In combination with the temperature change, MSPs are believed to be related to several mesospheric phenomena. The most common way of researching the mesosphere is utilizing radars, rockets and satellite.

In situ measurements can only be done through rocket experiments. However,

due to the high velocity and related effects around the rocket, these experiments are difficult to conduct. Several rocket experiments have been conducted over the years, designed to measure meteoric dust particles and their properties(e.g Havnes et al. (1996); Rapp et al. (2003); Brattli et al. (2006); Robertson et al. (2014); Antonsen and Havnes (2015)); Asmus et al. (2017)). The majority of rocket experiments were made during the summer months, measuring ice covered MSPs. Observations by SOFIE onboard the AIM satellite measured extinction of sunlight due to particles in the mesosphere. The observations are inconsistent with extinction of ice particles, and suggest that the mesospheric ice was not pure ice particle (Hervig et al., 2012). This supports the theory that meteoric dust acts as condensation nuclei for ice particles. Dust is also believed to be related to radar echoes that are observed in the summer, Polar Mesospheric Summer Echoes (PMSE). These echoes appear because of inhomogenetises in the refractive index at wavelengths 50-225 MHz. Several simultaneous radar and rocket experiments suggest that dust particles are essential in the formation of PMSE. Similar echoes, called PMWE for Polar Mesospheric Winter Echoes are observed also during the rest of the year (Latteck and Strelnikova, 2015). It is still an open question whether (or not) PMWE are liked to the presence of MSPs.

2.3   Winter Echoes in the mesosphere

PMWE occur in the winter months at altitudes between 55-85 km. Over the years there have been several theories and hypothesis on how these echoes are formed. One of the leading theories for many years has been that PMWE are caused by neutral air turbulence resulting from gravity waves breaking. This theory is sufficient to explain the echoes observed with a 50 MHz radar. Observations done with 224MHz radars, show strength twice the order of magnitude as the echoes observed with the 50MHz. For stengths of this order, the turbulence theory is not sufficient to explain the echoes (Belova et al., 2005). Later, Kirkwood et al. (2006) suggested an alternative explanation, not including neutral air turbulence at all. Their theory was based on the observation of large horizontal speeds done with a 50MHz radar, involving highly damped ion acoustic waves generated by particle reflection of infrasonic sound waves. However, the similarity to PMSE, have lead to theories of MSPs being involved in the formation process. Through heating and EISCAT experiments Havnes and Kassa (2009) suggested the connection between PMWE and MSPs using the EISCAT VHF radar, because they find similar behavior that was previously observed for PMSE. To observe PMWE the electron densities must be high enough for a sufficient reflective index for radar to observe them. This is suggested as an explanation for the diurnal variations, with significantly increased occurrence during the day and increased occurrence at solar proton event

(Latteck and Strelnikova, 2015). In addition, neutral air turbulence is believed to cause the inhomogenities in the radar backscatter, like for PMSE.

/3

The SPID probe

The Smoke Particle Impact Detector (SPID) is a Faraday cup instrument designed to detect meteoric smoke particles in winter mesospheric conditions when they have sizes around ~ 1 to 10 nm. SPID is a newly developed instrument, that was first flown onboard the G-chaser rocket in January. This chapter covers the design and mechanics of the instrument.

3.1 Design

The first Faraday cup, DUSTY, designed at the University of Tromsø, was in 1994 by Havnes et al. Together with a more recently developed probe, MUDD, they have successfully measured ice embedded MSPs during several summer campaigns over the years. The last campaign was MAXIDUSTY in 2016, investigating the relation between dust particles and PMSE, launched from Andøya Antonsen et al. (2017). SPID is made with heritage from MUDD and DUSTY, designed for winter conditions. Figure 3.1 shows the finished design of SPID with scales and grid structure. The bottom is open to allow air to flow through, dragging particles along. The grids are designed to shield and attract the ambient plasma, allowing only dust particles to reach the middle plate.

SPID consists of four grids GT1, GT2, GB1 and GB2 and a middle plate (MP). All grids have bias potentials relative to the payload. GT1 has a +10 V potential, to shield out the ambient ions and attract the electrons, as described by Havnes
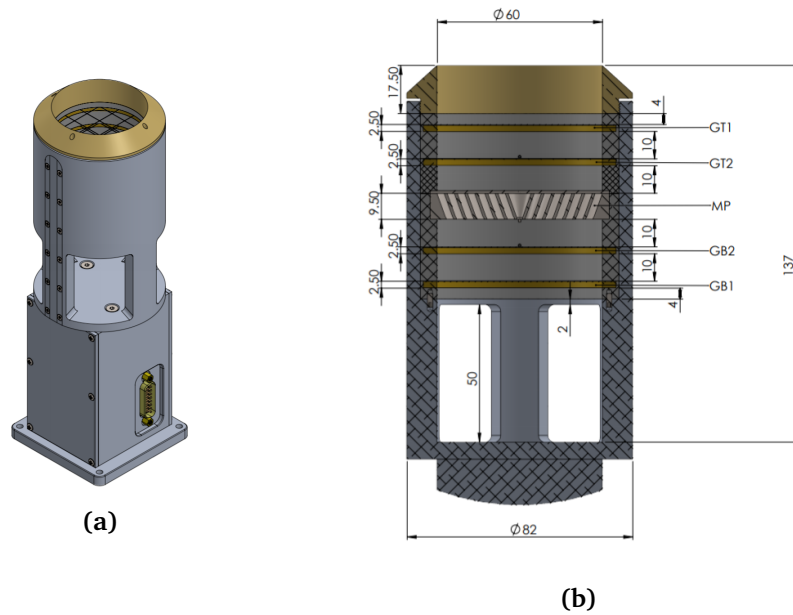
Figure 3.1: (a) Outside design of SPID. (b) Grid structure with scales in mm.

et al. (1996). The second grid, GT2, is set to a potential of -10 V, to oppose GT1, induce an electric field between the two, and attract the ions that are not stopped by GT1. MP has a bias voltage of -2 V, this was set to guide negative charge away from the plate, and attract positive particles. GB2 is set to +10 V, and GB1 to -10 V.
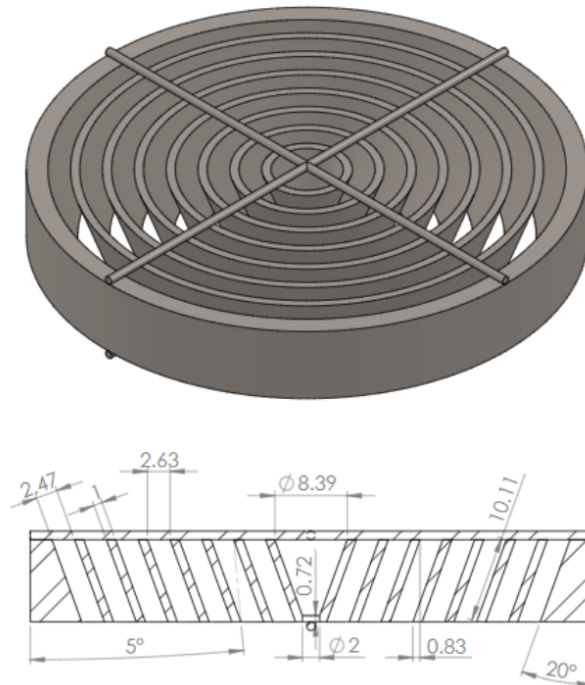
Figure 3.2: Close up middle plate design. Measures are in mm.

Figure 3.2 shows a close up design of the middle plate. It consists of 7 concentric rings with inclination of 20° to the perpendicular plane. The rings overlap slightly, so there is no transmission, and the chance of particles colliding with the middle plate grid is higher. The MP had the same design for SPID as for MUDD. The concentric rings with a tilt was designed to prevent free flow through the probe, and all incoming particles would hit the plate in the case for MUDD The MP design is identical to that of MUDD, preventing free flow through the probe, and all incoming particles would hit the plate (Antonsen and Havnes, 2015). SPID is designed for smaller particles, that can follow the steam, and opening the bottom increases the flow. However, the tilt results in no direct flow through the probe, except for the small opening in the middle. This increases the probability of particle collisions and interaction with the middle plate.

The detecting part of the probe has a height of 0.0137 m, on top of the electric part, reaching a total height of 0.0251 m. SPID was intentionally designed to be high, to reach the bow shock of the rocket itself. Combined with the

open design, a smaller fraction of the particles will be deflected, increasing the detection probability. More details on this in chapter 5. The grids consist of 10 0.25 mm silver wires, five and five crossing each other perpendicularly. The probe itself has a radius of 30 mm, which gives a complete cross-section of σ_{SPID} =28.37 cm^2, and each grid covers 4.6%.

Choosing the right material is vital in Faraday probes. Its the conducting surface that allows for detection, and several metals are suitable. In the case of SPID, the four metals used for the conducting surfaces are stainless steel, brass, silver and aluminium. POM Acetal Copolymer is used to isolate the grids. The four shielding grids consist of a 0.25 mm silver covered copper thread, connected to a brass ring, based on size and suitable to attach to the brass ring. For the middle plate, the choice fell on stainless steel, AISI 316L. It has a good corrosion characteristics, and oxidation coating will likely not form on the surface. The chosen materials were made to lower the probability of pollution from the instrument itself.

The design of SPID is such that particles enter the probe due to the airflow. This requires SPID to be placed on the top deck of the rocket, exposed to the flow induced by the rocket motion. The team from the University of Tokyo (PARM) also had one of their instruments on the top deck. The final configuration of the top deck, including the PARM instrument and the assembled SPID probe, can be seen in figure 3.3.

The electronics for SPID was designed by students at the electronics department at UiT Campus Narvik, together with Sveinung Olsen, senior engineer at the department of physics. The five grids were connected to amplification boards followed by the elbox. Telemetry limitations resulted in a sampling period of 0.0007 s, or as frequency, $1.4286 \cdot 10^4$ Hz. An average velocity of 1400 m^{-1} at mesospheric altitudes, gives a resolution of 1 m. However, inferring Shannon's sampling theorem, limits the resolution 2 m. The theorem states that for reconstruction of a continuous signal, samples must be taken at a frequency twice the original sampling frequency, to avoid aliasing.
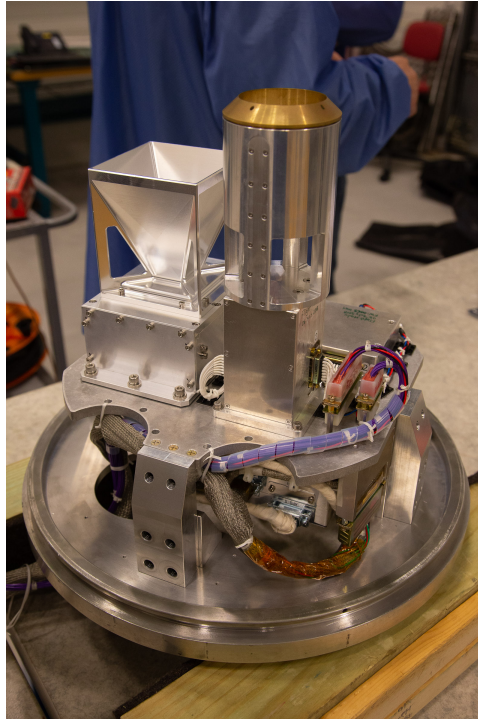
Figure 3.3: View of the integrated top deck. SPID is located of the center next to PARMs instrument.

3.2   Detection

SPID is designed to make use of the triboelectric effect, which s the tendency two conducting materials have to exchange charge. The grids are designed to shield ambient plasma from entering the middle plate. The incoming dust exchange charge with the grids and middle plate. In previous faraday cup probes, the secondary chagring effect has been observed, detailed explanation in Havnes and Næsheim (2007) and Havnes et al. (2018). This effect is a dust particles tendency carry electrons away from the middle plate, resulting in an observed positive current. Charged particles can also result in a current by hitting the grids or middle plate directly, and deposit all their charge onto the grid.

The middle plate is meant to serve as the primary detection plate. Neutral and positive particles could attract electrons from the middle plate, removing the charge, resulting in an observed positive current. Both negative and positive particles could hit the middle plate directly, and deposit their origi-

nal charge directly onto the grid. The charge exchange on the middle plate depends on the work function of the particles compared to the middle plate metal characteristics. In addition, the velocity and the radius of the incoming particle will effect the charge exchange. In a parallel master thesis, by Tinna Gunnarsdottir a detailed analysis of the charge exchange specifically for SPID is described.

Equation 3.1 states one way in which the current is related to the number density of dust particles, based on the work of Sagalyn et al. (1963), Havnes et al. (1996) and personal communication with Havnes. The current generated is dependent on the amount of particles present, times the charge they carry. The particle amount is estimated using the volume a rocket traverse in 1 second, times the number density of the particles. The volume can be estimated by $\pi * r_p^2 * v_r$ where r_p is the probe radius and v_r is the rocket velocity. The current will then be the amount of charges q generated. *eta* will here refer to the charge production efficiency, dependent on the radius of the particle. Not all particles will reach the middle plate, and furthermore, not all will hit the middle plate. To account for the loss of particles, the current is multiplied with an effective cross section σ_{eff}. Details on the estimations of η σ_{eff} will be presented in the following chapter.

$$I = \pi r_d^2 v_r N_D Z_D q \eta \sigma_{eff} \tag{3.1}$$

3.3 Testing

Prior to shipping SPID to Wallops for integration, several tests related to the electronics were conducted.

Several of the team members travelled to Wallops Flight Facility in August to be part of the final integration and test procedures. The first test we conducted in Wallops showed that one of the grids had malfunctioned, possibly as a result of the transport. By changing the recording channel, we fixed the problem. The rest of the grids worked as they should, with steady bias potentials. SPID passed the integration with Wallops' telemetry system.

The instruments were not switched on during the vibration test, but doing a sequence testing after, showed that SPID was still working as it should. When arriving at Andøya, all teams conducted individual tests on their instrument prior to the full sequence testing. The sequence testing was conducted in a steady location, and all five grids were measuring currents very close to zero.

Looking into the data after the test, showed, there was a small error when sampling values close to zero. There was no time to correct the error but it was taken into account during the processing of the data.

There was no time to conduct plasma testing on the probe. In the future a plasma test on a new model of the probe, could be helpful in the analysis of the retained data from SPID.

/4

Models used for analysis

Understanding the complex rocket dynamics and its effect on SPID, is essential in understanding the measurements. In this chapter the models used for analysis of the data will be presented. The first five sections describe the motion of particles and ions, due to the neutral air flow and shielding potential. Section 4.5 explains how the simulations of the particle trajectory, combined with distribution models can be used to estimate the effective cross section, and charge probability in the probe. The last section 4.7 describe the methods used for spectral analysis of the signal.

4.1 Neutral air flow

Estimation of the detection probabilities of different particle radii based on neutral airflow simulations has been done prior to the launch, presented in previous work by (Pineau, 2017). New simulations, accounting for the neutral density at the specific launch day and accurate rocket velocity, will be presented in this thesis. These will give estimates of the effective cross-section of the probe, which in term are used to give a more accurate estimation on the particle density.

As a rocket traverse upwards in the atmosphere, it will move through different flow regimes. Characterized by the degree of rarefaction in the neutral gas, the Knudsen number K_n describes the different flow regimes. The Knudsen

number is the ratio of the molecular mean free path λ and the characteristic length scale L of the system (Yunus, 2014). The definition of the mean free path in the atmosphere is:

$$\lambda = \frac{1}{\sqrt{2}\sigma_g n_g} \tag{4.1}$$

where n_g is the neutral air density and σ_g is the mean collisional cross-section, which for air molecule is $\approx 4.3 \cdot 10^{-19} m^2$. When $K_n \leq 0.1$ the gas is defined as a continuum flow. Disregarding the atomic nature of the gas is consistent with regarding the gas as continuous and homogeneous (Yunus, 2014). Continuum flow can be described by conventional fluid dynamics, following the Navier-Stokes equations with corrections for perturbations in the velocity distribution, possible to solve numerically using conventional computational methods for fluid motion (Hedin et al., 2007). When the Knudsen reaches numbers well above 10, the gas follows a free molecular flow. Analytical solutions for such flow are possible, with the assumption that individual molecules have collisionless paths. The problem arises when dealing with flows in the transition regime, where the collision frequency is too high to be neglected and too small to be regarded as a continuum (Hedin et al., 2007). A good method for studying rarefied gas dynamics is the Direct Simulation Monte Carlo (DSMC). The Monte Carlo simulation in this thesis has been conducted using the DS2V program developed by Bird (2005). The Monte Carlo method is a statistical used to simulate the two- and three-dimensional flow of the neutral gas. It gives a direct simulation of the microphysical processes in a gas flow as compared to conventional computational fluid dynamics. The derived neutral gas parameters estimated by the DSMC method are among others temperature, velocity and speed, pressure, density, particle density, mean free path and mean collision time. In addition, the simulation will indicate where the bow shock of the rocket will be.

4.2   Bow Shock

As the rocket traverses the atmosphere, it will compress the air molecules resulting in a higher density, dependent on the rocket velocity. The compression and density change of air affect the drag on the rocket and the motion of particles around it, resulting in a bow shock (Yunus, 2014). The bow shock standoff distance refers to the distance to which particles are affected by the object motion. The standoff distance is dependent on two variables; the Mach number M and the radius of the object r_{obj}, assuming that the ratio of specific

heats γ is $\sim$ constant. The Mach number describes the ratio of the velocity of an object, v_{obj} to the local speed of sound, c, stated in equation 4.2. It describes the comprehensibility effects and is used to define the flow regime of an object.

$$M = \frac{v_{obj}}{c} \tag{4.2}$$

The speed of sound can be given as $c = \left(\gamma \frac{k_B T_g}{m_g}\right)$, where k_4 is the Boltzmann constant, T_g and m_g is the temperature and mass of the gas respectively. The fluid flow regimes are, in regared to the Mach number defined as follows

- M < 1 Subsonic regime

- M = 1 Transonic regime

- 1< M <5 Supersonic regime

- M > 5 Hypersonic regime

Dependent on the flow regime of the rocket, some estimations of the standoff distance will not hold. The equation that will be used to estimate the bow shock standoff distance in this thesis is that derived by Farris and Russell (1994), that account for all Mach numbers. The relation between the standoff distance and the radius of the object is as:

$$\frac{r_{BS}}{r_{obj}} = 1 + 1.1 \frac{(\gamma - 1)M^2 + 2}{(\gamma + 1)M} \tag{4.3}$$

r_{BS} and r_{obj} represent the distace from the object to the standoff distance and radius of the probe, respectively. The Monte Carlo simulations of the neutral gas flow will also give estimates on the Mach number, and the standoff distance can be found by visual inspection of the flow results.

Equation 4.3 is from the definition of Farris and Russell (1994), where Λ is the standoff distance of the bow shock. R is the radius of the rocket.

4.3   Motion of neutral dust particles

The derivation of a neutral drag force term for dust particles, independent of flow regime, is described in the work of Antonsen (2013). It is based on the work of Baines et al. (1965) and Smirnov et al. (2007). The derivation is based on the assumption that the mass of the dust particles m_d are much larger than the mass of a gas molecule m_g. The velocity distribution of the neutral gas molecules is also assumed to follow the Maxwell-Boltzmann distribution. The last assumption is that the particles are spherical. The drag force can then be expressed as

$$
\vec{F}_D = \pi r_d^2 m_g n_g v_{th,g} (\vec{v}_g - \vec{v}_d) \frac{1}{u} \left\{ \frac{1}{\sqrt{\pi}} \left(u + \frac{1}{2u} \right) \exp(-u^2) \right.
$$
$$
\left. + \left(1 + u^2 - \frac{1}{4u^2} \right) \operatorname{erf}(u) \right\} \qquad (4.4)
$$

where $u = \frac{|\vec{v}_d - \vec{v}_g|}{v_{th,g}}$ is the normalized relative atom flow speed and $v_{th,g}$ is the thermal velocity, eq. 4.5 of the gas, where k_B denotes Boltzmann constant. The mass m_g, number density n_g, temperature T_g and velocity $\vec{v}_g$ of the neutral gas is estimated from the DSMC results.

$$
v_{th,g} = \sqrt{\frac{2 k_B T_g}{m_g}} \qquad (4.5)
$$

The temperature and size(mass) of the dust particle will change as it enters the probe. The energy equation 4.8, based on the work of Horányi et al. (1999) where P_N (eq. 4.6) is the heating due to collisions. Including an adjustment to account for dust particles, $\hat{P}_N$ (eq. 4.7), relates the mass change and the temperature change to each other. Radiation effects are neglected due to time restrictions.

$$P_N = \pi r_d^2 n_g v_{th,g} k_B T_g \tag{4.6}$$

$$\hat{P}_N = P_N \frac{1}{4} \left(\frac{2}{\sqrt{\pi}} (5 + 2u^2) \exp(-u^2) + \frac{1}{\sqrt{u^2}} (3 + 12u^2 + 4u^4) \mathrm{erf}(u) \right) \tag{4.7}$$

$$\hat{P}_N = \frac{4\pi}{3} \rho_d r_d^3 c_p \frac{dT_d}{dt} + L_d \frac{dm_d}{dt} \tag{4.8}$$

By combining equation 4.8 with kinetic theory, equations 4.9 and 4.10 can derived. These are the time evolution of the temperature and radius respectively For the full derivation, see Antonsen (2013).

$$\frac{dT_d}{dt} = \left(\hat{P}_N - L_d \cdot 4\pi r_d^2 \left(\frac{m_D}{2\pi k_B T_d} \right)^{\frac{1}{2}} \cdot P_{vap}(T_d, r_d) \right) \bigg/ \frac{4\pi}{3} \rho_d r_d^3 c_p \tag{4.9}$$

$$\frac{dr_d}{dt} = - \frac{P_{vap}(T_d, r_d))}{\rho_d} \left(\frac{m_D}{2\pi k_B T_d} \right) \tag{4.10}$$

where L_d is the latent heat vaporization, c_p is the spesific heat and ρ_d the mass density. $P_{vap}(T_d, r_d)$ denotes the vapor pressure for dust particles given as

$$P_{vap}(T_d, r_d) = P_{vap}(T_d) \exp \left(\frac{2\gamma m_D}{\rho_d k_B T_d r_d} \right) \tag{4.11}$$

$$P_{vap}(T_d) = 1.51 \cdot 10^{12} \exp \left(-\frac{56655}{T_d} \right) \tag{4.12}$$

Table4.1 gives the description on all the constants and their value for smoke particles.

The motion of the dust particle can be described by Newtons second law. The forces acting on the particle are the gravitational force, the electric force and the neutral drag force. The latter is explained in the beginning of this section. The gravitational force is by definition $\vec{F}_g = m_d \vec{g}$, and the electric force

$\vec{F}_E = qE$. The gravitational constant g is set to 9.8ms^{-2} and the electric field will be estimated with the electric field solutions, more details in the following section.

$$m_d \frac{d\vec{v}_d}{dt} = q_d \vec{E} + \pi r_d^2 m_g n_g v_{th,g} (\vec{v}_g - \vec{v}_d) \frac{1}{u}$$
$$* \left\{ \frac{1}{\sqrt{\pi}} \left(u + \frac{1}{2u} \right) \exp(-u^2) + \left(1 + u^2 - \frac{1}{4u^2} \right) \mathrm{erf}(u) \right\} \qquad (4.13)$$

$$(4.14)$$

The particle trajectory and dynamics due to the internal conditions of the probe can now be described by the coupled differential equations 4.9, 4.10 and 4.14. These can be solved using numerical analysis like the Runge Kutta. The model requires initial conditions, which in this case is initial particle radius, velocity, temperature, position and the charge state of the particle.

This method only includes the motion of charged particles, and in the following chapter the method of solving the electric field within the probe is explained.

Table 4.1: Constants in particle trajectory simulation. Figure adapted from Antonsen (2013)

Parameter	Description	Value
ρ_d	MSP mass density	3000 kgm^{-3}
m_D	Mean dust weight,	140 amu
L	Latent heat vaporization of MSP	$6 \cdot 10^6$ Jkg^{-1}
c_p	Specific heat of MSP	1000 Jkg^{-1}K^{-1}
$\bar{\gamma}_{MSP}$	Mean surface energy	0.200 Jm^{-2}

4.4 Electric field simulations

All grids on SPID have biased electric potentials, as discussed in chapter 3. The theory is that these grids will contribute to shielding/attract ambient plasma, allowing only dust particles to reach the middle plate. The dust particles can also carry charge, and as a consequence, they will be affected by the electric force from the induced electric fields.

Due to the complex structure of SPID, numerical methods must be applied

to describe the electric fields inside the probe. Considering the rotational symmetry of SPID, symmetric solutions can be applied, which simplifies the calculations. Equation 4.15 is Maxwell first equation, also known as Gauss' law, on differential form. It states that the divergence of the electric fields equals the total charge density, ρ divided by the permittivity of free space ε_0.

$$\nabla \cdot \mathrm{E} = \frac{\rho}{\varepsilon_0} \tag{4.15}$$

By definition the relation between the electric field and potential is given as $\mathrm{E} = -\nabla V$. Usign this in eq 4.15 gives Poisson's equation 4.16

$$\nabla^2 V = \frac{\rho}{\varepsilon_0} \tag{4.16}$$

Two assumptions have been made, to solve equation 4.16 for SPID; (1) No space charges in the background gas. The validity of this assumption will be discussed in detail in chapter 5. (2) Rotational symmetric solutions are allowed due to the spatial configuration of the probe. Equation 4.16 now reduces to the Laplace equation, given in cylindrical coordinates:

$$\frac{1}{r}\frac{\partial}{\partial r}\left(r\frac{\partial V}{\partial r}\right) + \frac{\partial^2 V}{\partial z^2} = 0 \tag{4.17}$$

This will give the azimuthally symmetric solution of the potential, for r and z (Antonsen, 2013).

Equation 4.17 can be solved numerically by applying a finite element method (FEM). Dirichlet boundary conditions are applied, specifying the electrostatic potential at the boundaries, which for SPID will be the bias potentials. FEM involves meshing the geometry into small triangles, and solving the differential equation for each triangle. The results can be exported and used to derive the electric field for singular points withing the probe.

As a simple check for the accuracy of the method, the results are compared to the static solution of a homogeneous electric field between two infinite sheets, given as

$$E = -\frac{\Delta V}{d} \tag{4.18}$$

where d is the distance between each grid. Another check that will be done, is investigate the plasma effects. In the simulations it is assumed no space charges. This is not valid for plasma, as the field will drop off faster, resulting in less shielding effect by the grids.

4.4.1   Electric field in plasma

In order to estimate the motion of dust in the detection the plasma conditions must also be considered. In a plasma, ions and electrons exist separate. For something to be called a plasma, three criteria must be fulfilled; (1) The amount of particles must be sufficient for shielding to occur. (2) The plasma frequency must be much higher than the collision frequency, $\omega_p \gg \omega_c$. Where the plasma frequency is defined as

$$\omega_{pe} = \left(\frac{n_e q^2}{\varepsilon_0 m_e}\right)^{1/2} \tag{4.19}$$

The third requirement is that the characteristic length scale of the plasma, the Debye length λ_D, defined as

$$\lambda_D = \sqrt{\frac{\varepsilon_0 k_B T_e}{n_{e,0} e^2}} \tag{4.20}$$

must be much shorter than the dimension of the physical system L, $L \gg \lambda_D$. A fourth requirement that somewhat goes under the other three is quasi-neutrality, $N_i \simeq N_e$ (Bittencourt, 2013). Shielding of electric potentials applied to a plasma is one of the fundamental characteristics of a plasma. In free space, the potential can be given as

$$\phi(r) = -\frac{e}{4\pi \varepsilon_0 r} \tag{4.21}$$

where e is a unit charge and ε_0 is the vacuum permitivity. In a plasma there is an additional exponential factor due to the Debye shielding (Chen, 1984).

$$\phi_p(r) = -\frac{e}{4\pi \varepsilon_0 r} \exp\left(-\frac{\sqrt{2}r}{\lambda_D}\right) \tag{4.22}$$

The potential decay becomes significant when the distance r is approaching the Debye length.

4.5 Detection and charging probability

The ultimate goal of the SPID instruments, is to use the current measured to obtain dust parameters such as the dust flux and radius. SPID is a completely new instrument, and the methods derived by Havnes et al. (1996) does not apply exactly. Chapter 3 covers the details of SPID, and how the current relates to the number densities. The current generated depends on the dust flux into the probe. This is accounted for in a correction factor of the cross section, here referred to as the detection probability.

A model is presented to estimate the detection probability at specific altitudes, by combining the particle trajectory simulations and size- and charge distribution models. The particle trajectory depends on the radius and charge of the dust particle, as discussed in section 4.3. These will effect the cross section. Using model estimates of the dust distribution give ratios relative to charge and radius. Equation 4.23 can be applied to estimate the effective cross section of the probe. c denotes the simulation results as a M times N matrix, where M is the number of charge states and N is the number of initial radii. The matrix contains the fraction of particles hitting or passing the middle plate. The cross section is defined as $\sigma = \pi r_p^2$, and to This will account for the 2 dimensional geometry the c matrix is in the power of 2. $\zeta_{i,j}$ is a M times N matrix containing the charge probability for each radius, i.e the fraction of a negative charge with radius r_i, to a positive charge radius r_i. Each column sums to 1. β_j is a 1 time M vector containing the radius probability, i.e the probability of a particle having a radius r_1 compared to r_2. The vector sums to 1. 4.2 show an example matrix of β and η.

$$\sigma_{eff} = \left(\sum_{i=1}^{N} \sum_{j=1}^{M} c(i,j)^2 \zeta_{i,j} \beta_j \right) \tag{4.23}$$

Table 4.2: Example of the charge β and rasius ζ probability distributions matrixes

β		N		
		1 nm	2 nm	3 nm
	q	0.7	0.3	0.2
M	0	0.2	0.5	0.6
	-q	0.1	0.2	0.2

ζ	0.1	0.3	0.6

Estimates of the charge transfer from MSPs to the middle plate can be used as reference charge number η_{ref} and radius r_{ref}. The charge number η can then be estimated as

$$\eta = \eta_{ref} \left(\frac{r_d}{r_{ref}} \right)^2 \tag{4.24}$$

where r_d is the dust radius (Havnes and Næsheim, 2007).

4.6   Ion contribution

Since the drag force is derived based on the assumption that the mass of the particle is much larger than the mass of one neutral gas molecule, it does not apply for ions. Ions are of sizes comparable to the neutral gas. The dynamical motion of them, will not follow the same drag term as the larger dust particles. SPID is designed with an open bottom, and combined with the high velocity of the rocket, the flux of particles into the probe will most likely be higher than anticipated, thus ion motion must be considered.

In section 2.1.1 the most abundant ion species in the mesosphere are mentioned. These have masses ranging from 16 to 100 a.m.u. In addition there exist water cluster ions, that can have masses up to 400 depending on number of water molecules. This is around the same mass as a dust particle with a radius of 4 Å.

Here the motion of the ions will be considered in two ways, first only the thermal energy will be compared to the shielding energy of the probe. In this case, the neutral-ion collision is completely neglected. The other evaluation will be on the collision frequency of the ions, compared to the spatial distance

they will travel.

The thermal velocity or speed of an object is defined as the motion of the object due to the thermal conditions

$$v_{th} = \sqrt{\frac{2k_B T}{m}} \tag{4.25}$$

The kinetic energy from this motion can be defined as the thermal energy with the formula $\frac{1}{2}mv_{th}^2$. A potential can be converted directly to eV by definition.

The second consideration that will be made is the ion-neutral collision frequency. The simplest way of estimating it is by assuming that the neutral density is much higher than the ion density, which leads to the collision frequency being determined by the neutrals. The neutral collision frequency will be given by the DSMC results. Brekke (2013) defines a theoretical ion-neutral collision frequency as

$$\nu_{in} = 2.6 \times 10^{-15}(n_n + n_i)(M'_n)^{-1/2} \tag{4.26}$$

where the neutral and ion densities are n_n and n_i respectively, and M'_n is the mean molecular mass.

Estimating the momentum transfer between the ion and neutral collisions, and compare that to the gained energy to that of the ions. This will give an estimate of how many collisions an ion requires to overcome the shielding potential.

$$m_n v_n + m_i v_i = m_n v'_n + m_i v'_i \tag{4.27}$$

4.7 Spectral analysis

Rockets move from subsonic to supersonic velocities, resulting in a substantial amount of strong forces acting on them. Torque is a term used for the rotational

effect of a force on an object. The torques act on the rocket contributes to making the rocket unstable — making the rocket spin will stabilize the rocket by minimizing the effect of the torque. The spin asures that the rocket follows the predicted trajectory. There are several ways to infer a spin. On small rockets, it is sufficient to use fins on the boosters, as was done with the G-chaser rocket (on larger rockets, a fin might not be adequate, and extra boosters are required). The spin will be more or less constant but may vary some over the trajectory.

On scientific rockets, the spin can be a problem for the experiments. A despin is used to slow down the spin of the rocket, allowing experiments to measure a specific volume for a longer time. A yo-yo despin was used for G-chaser, initiated 70 s after launch, corresponding to an altitude of $\sim 80 km$

Over the decades' rocket experiments have been conducted, several measurements show an apparent effect by the spin of the rocket ((Yau et al., 1981), (Kurihara et al., 2006), (Havnes and Næsheim, 2007),(Antonsen, 2019)). Why these effect appears, relies on a range of factors, and highly depends on how the instrument is designed, and what is to be measured. In several Faraday cup instrument the rotational effect has also been observed. Explanations of the effect is related to the change of particle flux.

Analyzing the rotational effects, and accounting for them can be done in several ways, dependent on what is to be achieved. This section describes how Fast Fourier transform and Wavelet Analysis has been used to determine the frequency components and time dependence on the signal.

Fast Fourier Transform

The Fourier Transform is a method of displaying the underlying frequency components of a signal. The Fast Fourier Transform (FFT) was an optimization of the traditional Fourier transform, making it more applicable to digital signal processing such as spectral analysis, Fourier spectroscopy, image processing, and the solution of differential equations. FFT computes the discrete Fourier transform of the signal, converting the signal from its original domain, usually time or space, to it frequency domain. For a vector x with n uniformly distributed sample points the FFT is defined as:

$$y_{k+1} = \sum_{j=0}^{n-1} \omega^{jk} x_{j+1} \qquad (4.28)$$

where $\omega = e^{-2\pi i/n}$, and n is one of the complex roots of unity and i is the imaginary unit. j and k can range from 0 to $n-1$ (Cooley et al., 1969). By taking the FFT, the frequency components of the signal will be visible, in terms of amplitude of the spin components. The FFT can also give an approximation of the power spectrum by multiplying with its complex conjugate.

Wavelet Analysis

The weakness in a Fourier transform is that some information is lost in the transform. Most often you lose information of the original domain, i.e time stamp or spatial position of the signal. Sliding averaged Fourier transform, keep some information on time, but is limited in resolution. The wavelet analysis is designed to keep information on the time component in addition to obtain information on other components (Chun-Lin, 2010).

Torrence and Compo (1998) describe the practical use of the wavelet transform. Wavelet analysis is set up as a convolution of a time dependent signal x_n and a scaled and translated version of the wavelet function $\Psi_0(\eta)$:

$$W_n(s) = \sum_{m=0}^{N-1} r_m \Psi^* \left[\frac{(m-n)\delta t}{s} \right]$$ (4.29)

where W_n is the resulting wavelet spectrum. ψ^* denotes the complex conjugate of the wavlet function. The time signal, x_n must have equal spacing, δt and has localized time indexes n = 0 ... N-1 (Torrence and Compo, 1998). s is the dilation parameter, corresponding to scale length or temporal period, and is always a real number larger than zero. The convolutions are done by varying s and translating it along n, which transforms the one-dimensional time series into the two-dimensional parameter space (s,n). It also gives a local measurement of the relative amplitude of the activity scale at scale a at time b Meyers et al. (1993).

For $\Psi_0(\eta)$ to satisfy the requirements of the wavelet function, it must be localized in time and space and have a zero mean. Here we will consider the Morlet Wavelet, consisting of a plane wave modulated by a Gaussian, depending on the nondimensional time parameter η, and ω_0 is the nondimensional frequency:

$$\psi(\eta) = \pi^{-\frac{1}{4}} e^{i\omega\eta} e^{\frac{\eta^2}{2}}$$ (4.30)

When evaluating finite-length time series, boundary effects, or edge effects, will occur in the beginning and end of the wavelet power spectrum. This effect occur because the at the edges, data are inevitably assigned outside the range of values. There are several way to account for these edge effects. However, using the edge data should be done with caution. For the wavelet transform the edge effects are accounted for in the cone of influence (COI). According to Torrence and Compo (1998) definition, the e-folding time is used to delineating the egde effects. They define $\sqrt{2}e$ as the cone of influence for a Morlet Wavelet.

From the wavelet analysis information on the power spectral density (PSD) may also be obtained, by $|W_n(s)|2 = WW*$ where (*) denotes the complex conjugate. This PDS will be arbitrarily formalized. By inspecting the PSD, the slopes of the signal will be evident, and possible to compare to theory, see section 2.3.

5

Simulation results

In this section the simulations of the dynamical effects on dust particles and ions are presented This chapter summarize the simulations and considerations made regarding the dust particle motion and ion motion, theory explained in chapter 4. The simulations are based on previous work done by Tarjei Antonsen, Adrien Pineau and myself, but changed and improved to correspond with the launch conditions and final design.

5.1   Neutral air flow

The neutral flow models were carried using the DSV2 program by Bird (2005). The simulations were conducted for three different altitudes. 55km 60km and 85km. This is in the limits of where dust particles usually are located in the winter mesosphere. The two close simulations were to see the difference over a short altitude. In addition, a significant enhancement between these altitudes can be seen in the raw current, figure 6.7. The neutral atmosphere input parameters were used from the MSIS-E_90 Atmosphere Model for mid January conditions (CCMS, 2019) and the rocket velocity (v_R) used from the flight data provided by NASA Wallops Flight Facility. The values are listed in figure 5.1. There is a significant difference between the lower altitude parameters and the higher ones. Temperature decreases by $\sim$ 50 K, and number densities decrease by $5 \cdot 10^{21}$.

Table 5.1: Initial values used for the DSMC simulation. Temperature and density from the MSIS model for 13th of January 2019.

Alt [km]	T [K]	N_D $\mathbf{m^{-3}}$]	$v_R[\mathbf{ms^{-1}}]$
55	255	6.6142×10^{21}	1620
60	247	3.47 ×10^{21}	1595
85	207	1.03 ×10^{20}	1464

Figure 5.2 shows the DSMC results from 60 km. The simulations were only conducted for half the probe, and then mirrored to display the entire flow. Simulations are done neglecting the other instrument, see figure 3.3. The effect of the PARM instrument has not been considered due to it being located ∼ 5 cm below the opening of SPID. It could possibly cause some turbulence effects on the flow, but should not effect the flow of the particles entering form the top. Figure 5.2a displays the number density of the neutral gas. It shows that the increase in density inside the probe is on the order of ∼ 2. In comparison to the MUDD instrument, with a closed bottom, the shock front is significantly decreased. Consistent with theory and previous simulations on open bottom probes (e.g Hedin et al. (2007); Pineau (2017)). The density is homogeneous within most of the top half of the probe. Close to the probe walls, there are inhomogeneties, as a result of edge effects. A notable feature can be seen in the opening in the center of the middle plate, where the number densities reach values of ∼ $7 \cdot 10^{22}$. Figure 5.2b shows the simulated neutral gas temperature. Inside the probe the temperature increases by a factor of ∼ 10^2. Using the temperature change across an oblique shock with Mach number of 5 gives and estimated temperature increase of ∼ $1500K$, close to the simulation results. The high temperature increase is a result of the high velocity of the rocket. Figure 5.2c shows the speed of the neutral gas. The particles loose momentum when entering the probe as a result of passing the shock front, and the velocity is decreased by a factor of 10. On the top side of the MP the Mach number is ∼ 0.3, within the subsonic flow regime. When the flow pass the middle plate grid, heat is transferred to the gas, resulting in an increase in the Mach number to ∼ 1 after the particle pass the MP grid.

Simulations were also carried out for altitudes of 55 and 85 km. There is little change between 55 and 60 km, except for an increase in the number density and small changes in the temperature and velocity components. The flow structure inside the probe is similar for all altitudes, but the flow is increased and edge effects stronger due to the higher velocity and number densities at lower altitudes. The shock front increases with altitude, as a result of decrease in rocket velocity. The results of the DSMC results for 85 km can be found in the appendix.

A simulation was done including the nosecone deck, to see the entire shock front of the rocket. Following equations 4.3 gives an estimated stand off distance ratio at 60 km to be 1.095 with a Mach number of 4.952. The payload radius is 0.2192 m, which gives a stand off radius of 0.24 m. The scalar pressure of the full nose cone deck for an altitude of 60 km can be seen in figure 5.1. This illustrates better the bow shock of SPID, corresponding to the values from the theory.
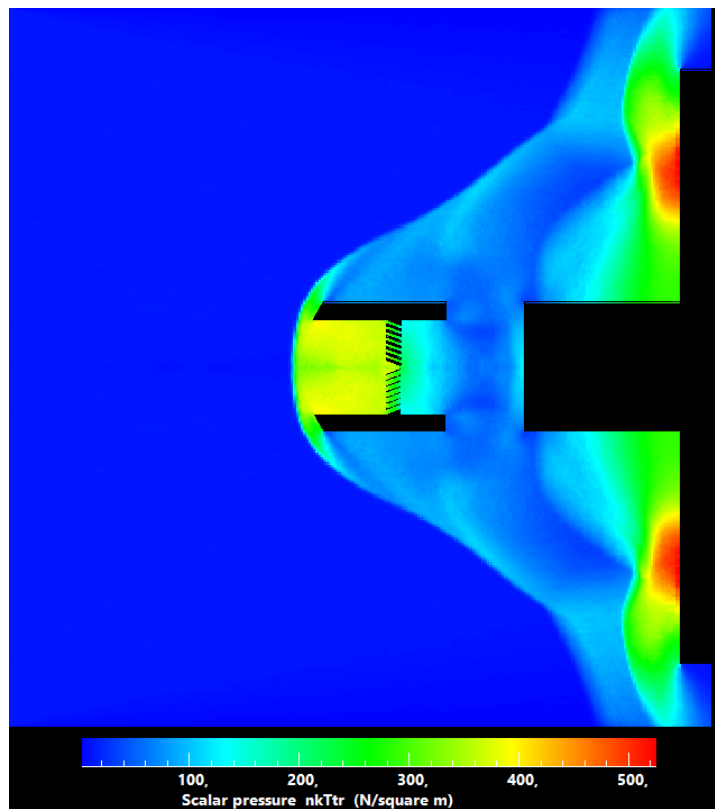
Figure 5.1: DSMC results of the neutral gas flow for the entire top deck at 60 km.
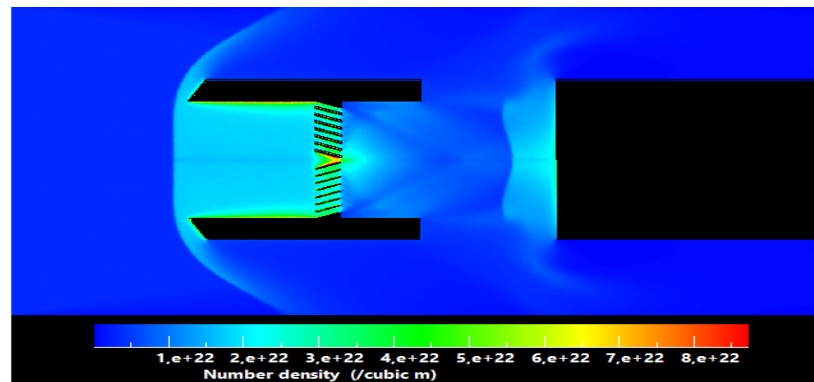
(a)
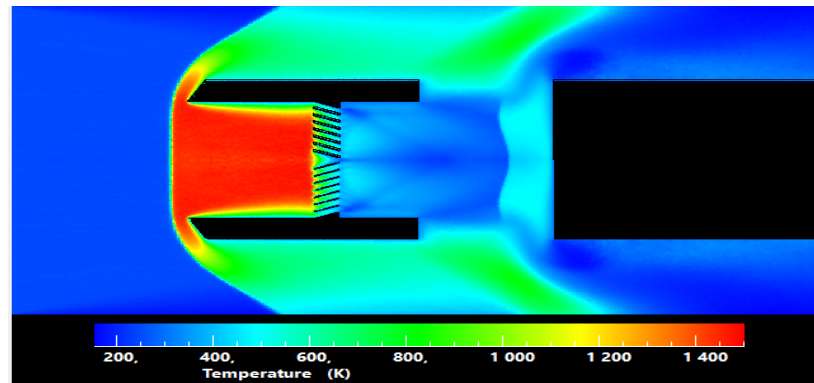
(b)
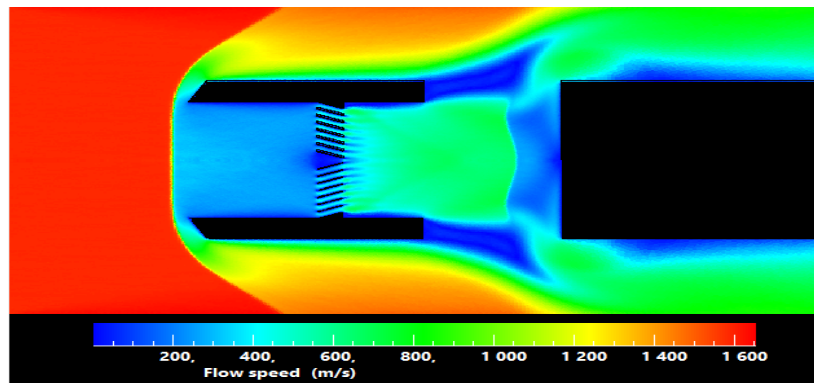
(c)

Figure 5.2: Results from DSMC for 60 km for neutral gas flow. (a) Number density per cubic meter. (b) Temperature in Kelvin. (c)Speed in meters per second

The instrument design combined with the rocket velocities result in a sig-

nificant decrease in bow shock, decreasing deflection of small particles. The temperatures inside the probe increases substantially due to the rocket velocity, with Mach number of ~ 5. The tilted design of the middle plate results in a large acceleration of the particles as a result of heating within a subsonic flow. With increasing altitude the shock front increases due to the decreasing velocity. The drag force on the particles is dependent on the gas velocity and the neutral gas density, in addition to the thermal velocity of the neutral gas, see equation 4.4, all in which decreases with altitude.

5.2   Electric field solutions

SPID consist of 5 potentially biased grids, which will induce an electric field. The method of determining this electric field is presented in section 4.4.1. In this section the results of the 2D simulations using FEM are presented. The relative permitivity, ε_0 is set to unity, assuming no space charges. The validity of this assumption is discussed in the end of this section.

The simulations were first done for the standard bias settings, assuming the payload potential is zeros. Calculations are made for the entire probe, both for the potential and the electric field. The potential variations can be seen in 5.3.
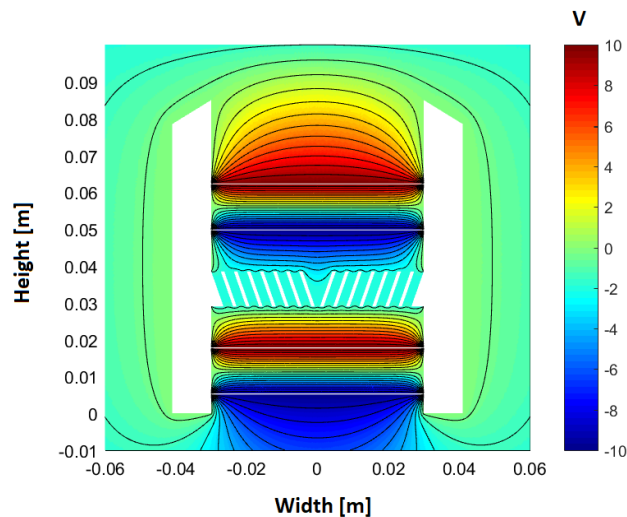
Figure 5.3: Potential contours of SPID in the case of no space charges.

Figure 5.4 show the absolute value of the electric field results. Strong edge effects occur were the grids are attached to the probe structures and at the edges of the middle plate. The colorbar has been re-scaled to account to show variations of the field inside the probe. Original maximum value was $\sim 10^4 \cdot 10^4$. Between GT1 and GT2, as for GB1 and GB2, the simulations give a field strength of 1633 Vm^{-1} away form the edges. This corresponds almost exactly with the estimated potential in the case of infinite conducting planes. Looking at the potential structures in 5.3, the potential varies homogeneous between the two plates, consistent with the results. As one approach the edges, the electric field diverges from the static solution, and grows several orders of magnitude. At the edges, as seen in 5.1, turbulence cells appear, also contributing to the motion of the particles. If these fields can actually grow to sizes of $\sim 10^4$, depends on the fine mechanical construction of the probe.
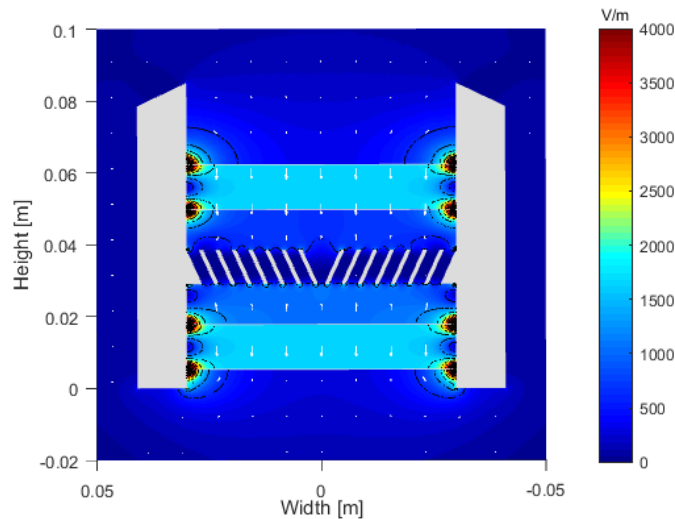
Figure 5.4: Electric field solutions, showing the contours and vector lines. The colorbar has been re-scaled, max value originally $6 \cdot 10^4$, due to edge effects.

The middle plate consist of seven concentric rings, and on the edges of each ring edge effects occur. This effects the potential between GT2/GB2 and the middle plate. In this region the field is less homogeneous. The field between GT2 and MP varies has a value of $\sim 650 Vm^{-1}$, $\sim 70 Vm^{-1}$ from the infinite sheet solution. GB2 and MP vary ~ 10 Vm^{-1}.

Studies suggest that a rocket becomes charged, as it acends in the atmosphere due inhomogenities and wake effects around it (e.g Miloch (2010) Darian et al. (2017). Studies suggest that the negative charge of the payload is more significant than the positive Brattli et al. (2006). The bias potentials are set

relative to the payload charge. In effect, as the payload become more negatively charged as it traverse the atmosphere, the shielding potential on the top grid will decrease. The grids are all biased relative to the payload, thus the induced electric field between the grids will not be changed. However, this effect have proven to be more significant at higher altitudes,

The simulations correspond with the theoretical estimates. Strong enhancement of the field around the edges. As a result the accuracy of the drawn geometry.

5.2.1   Electric field in plasma

The shielding efficiency of the grids are depending on how fast the electric field drops off. This depends on the Debye length, see 4.4.1. If the debye length is sufficiently large, the electric field will drop off as a point charge. However, if the Debye length is small, shielding will occur, and the electric field will drop off faster. The simulation on the electric field in the probe is based on the assumption that the rocket is operating in vakuum.

The Debye length is dependent on the electron densities. The rocket did not have an instrument measuring the electron densities or temperature. The electron densities used are from the model of Baumann et al. (2015), in addition to the EISCAT observations obtained from the Madrigal website. For lower altitudes both the UHF and the VHF have low resolution, so the densities are averaged over four sampling periods corresponding to $\sim$ 3 minutes. Figure 5.5a show the electron densities in m^{-3}.

The Debye length is inversely proportional to the relation electron density, following equation 4.20. Figure 5.5b show the ratio between the radius of SPID, 0.03m and the calculated Debye length. This tells us in which regime the probe is operating. At lower altitudes, the ratio is low, indicating that the probe is well withing the shielding sphere. In effect the electric field will decay as a r^{-1}. For higher altitudes the ration increases, i.e. the Debye length becomes smaller, and the particles are shielded. It should be noted that the Baumann Debye length is calculated with a constant temperature set to T = 250, since there is no corresponding temperature measurements. The temperature change is low compared to the Debye length over the altitude range considered, and thus should be close to the actual values.

The assumption that the probe is not operating in a plasma for low altitudes suggest to hold, the Debye length is large, and thus the exponential decay of the potential is small. The electric field simulations are done approximating the grids as thin sheets. Considerations on the 3D form and effect of the field

(a)

(b)
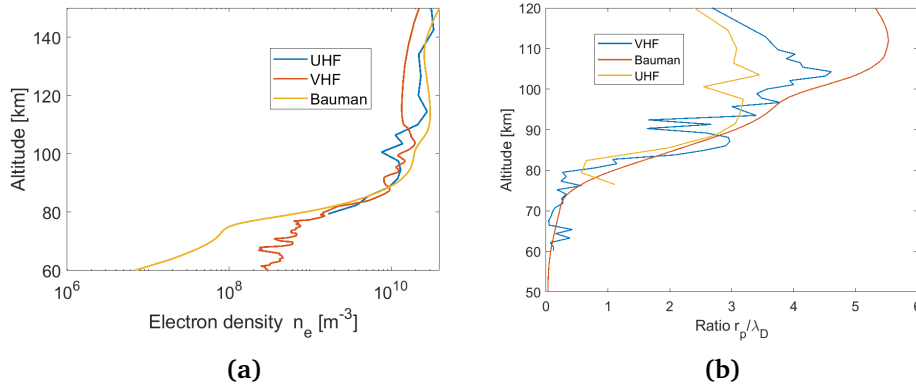
Figure 5.5: (a)Comparison of the electron densities obtained with EISCAT VHF, EIS-
CAT UHF and simulations done by Baumann et al. (2015). The horizontal
axis is on a logaritmic scale, and all densities are in m^{-3}. The values
correspond well up to an altitude of $\sim$ 100 km, where the simulations
overestimate the density. (b) Ratio of the radius of SPID and the Debye
length as a function of altitude.

distribution should be considered in future simulations.

5.3   Particle trajectory

By using the results from the DSMC and electric field simulations the trajectories
of the dust particle can be derived solving equation 4.14. It is solved using the
Runge Kutta method, with time steps of $dt = 4 \times 10^{-8}$. The time is set based
on the size of each cell from the DSMC (Pineau, 2017). The particles are set
to start at a height $\sim$ 0.03 m from the tip of the probe, so that the effects
prior to entering the probe can be observed. The initial horizontal position
is randomly generated when estimating the cross section. In the figures, the
initial positions are evenly spaced to better compare the internal effect of the
particles. For each radius and charge the simulation is done for 100 particles at
each run, and a total of three runs. From the results an estimate on the effective
cross-section of the grid can be determined. Assuming no initial horizontal
velocity and vertical initial velocity is set to the rocket velocity at $\sim 60 km$,
$v_r = -1590 ms^{-1}$. Positive direction is defined upwards.

Pineau (2017) studied the neutral dust flow of one of the early designs of SPID,
showing that particles of nm size would enter the probe, but for lower altitudes
around 60 km, the detection rate was bellow $\sim$ 30 %. His simulations were
done with a rocket velocity of 1000ms^{-1}, and did not account for the charged

particle motion.
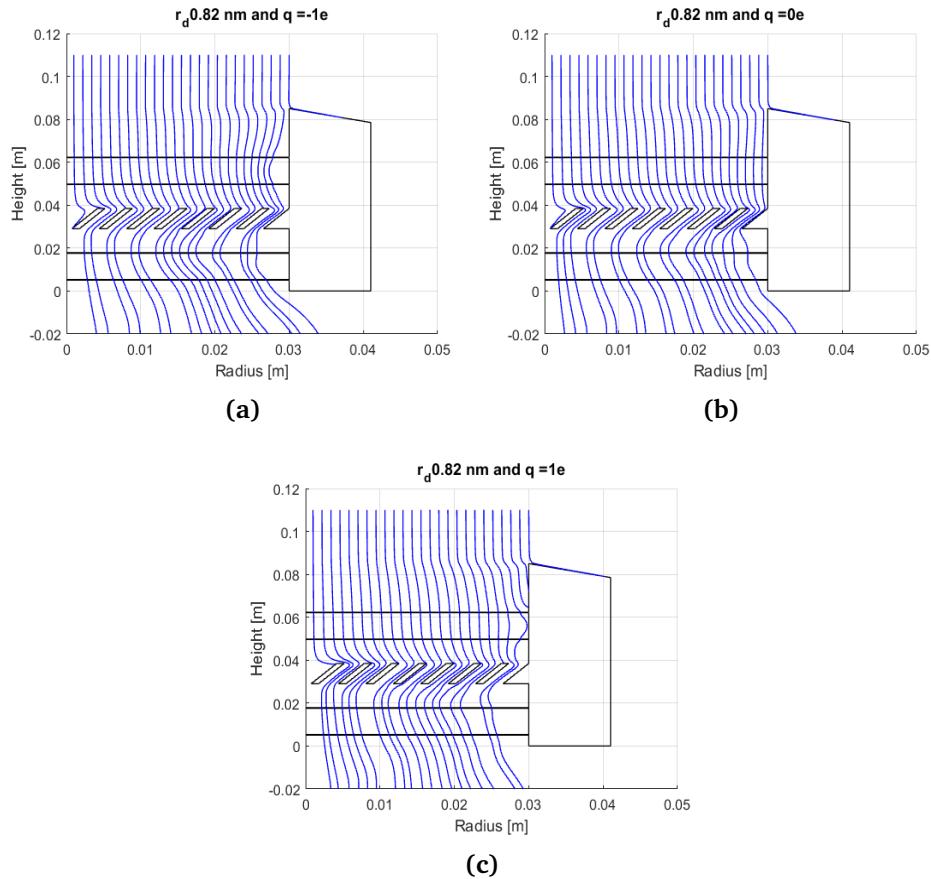
Figure 5.6: Particle trajectories of dust particles at 60 km with particles of radius 0.82 nm. (a) Trajectory for a negative particle. Close to the edge the particles are slightly bent as a result of the edge effects, see 5.3 (b) Trajectory for a neutral particle. Follows the flow as expected. (C) Trajectory for positive particles. The trajectories before the middle plate show small deviation from the neutral trajectory.

Figure 5.6 show the particle trajectories for negative, neutral and positively charged MSPs with a radius of 0.82 nm at 60 km. Most of the particles as can be seen are transported with the neutral air flow. In figure 5.6a for the negatively charged particles bulge from the walls. Looking at figure 5.3 which illustrates how the potential varies, the electric field will be stronger in the middle. Close to the edge there is an area where it drops off, which explains the positive trajectories in figure 5.6c. The positive particles entering the probe close to the edge are deflected and hit the probe walls. As expected the neutral particles follow the air stream, see figure 5.6b. Another effect present in all three

trajectories is in the middle plate center effect. Due to the opening it effects the air flow, and seen in figure 5.2c is that the neutral gas has close to zero speed, corresponding to a turbulent pocket. The simulation suggest that negative particles bellow 0.4 nm are efficiently attracted to the GT1 shielding grid. Positive particles bellow 0.3 nm are efficiently attracted to the GT2 shielding grid.

Table 5.2: Detection efficiency of the middle plate at 55 km, from simulations. Also includes estimates on the efficient cross section using formula 4.23

		Hit			Pass + hit		
		-q	0	q	-q	0	q
	0.5	0.0361	0.0324	0.0036	0.8649	0.9025	0.6084
	0.8	0.0484	0.0289	0.0121	0.9801	0.9409	0.7921
	1.3	0.0529	0.0324	0.0324	1.0000	1.0000	0.9025
r [nA]	2.1	0.0676	0.0441	0.0676	1.0000	0.9801	0.9604
	3.4	0.0961	0.0900	0.1444	1.0000	0.9801	0.9604
	5.4	0.1521	0.1600	0.2209	1.0000	1.0000	0.9801
	8.6	0.4761	0.4624	0.6241	0.9801	1.0000	0.9409
σ_{eff}			0.1			0.96	

Table 5.3: Detection efficiency of the middle plate at 60 km, from simulations. Also includes estimates on the efficient cross section using formula 4.23

		Hit			Pass + hit		
		-q	0	q	-q	0	q
	0.5	0.0961	0.0049	0	1.0000	0.8836	0.3969
	0.8	0.0324	0.0144	0.0016	1.0000	0.9409	0.6724
	1.3	0.0400	0.0324	0.0121	1.0000	0.9409	0.8100
r [nA]	2.1	0.0625	0.0576	0.0361	1.0000	0.9604	0.9025
	3.4	0.1444	0.1156	0.0961	1.0000	0.9801	0.9216
	5.4	0.6724	0.8100	0.5776	0.9801	0.9801	0.9604
	8.6	0.8649	0.9409	0.9604	1.0000	0.9801	0.9801
σ_{eff}			0.3			0.97	

Table 5.4: Detection efficiency of the middle plate at 85 km, from simulations. Also includes estimates on the efficient cross section using formula 4.23

		Hit			Pass + hit		
		-q	0	q	-q	0	q
	0.5	0	0.0676	0	0	0.9409	0
	0.8	0	0.0441	0	0	0.9801	0.5929
	1.3	0.1444	0.1089	0.0289	0.7921	0.9604	0.7744
r [nA]	2.1	0.6724	0.6241	0.7921	0.8464	0.8836	0.9025
	3.4	0.8836	0.8649	0.9025	1.0000	0.9801	0.9801
	5.4	0.8836	0.9604	0.9604	1.0000	1.0000	1.0000
	8.6	0.9801	0.9216	0.9604	1.0000	0.9801	0.9801
σ_{eff}			0.01			0.09	

Tables 5.2 - 5.4 show detection efficiency estimated from 100 particles with random start position between 0 - 0.03 m. Each particle position is done for positive, negative and charged, and radii from 0.5 to 8.6. Hit shows the detection rate when only the particles hitting the middle plate directly are considered. Pass + hit includes all particles that pass and hit the middle plate. The charge exchange process for dust particles is not yet well understood. Charge could be generated when the particles impact directly, and by coming sufficiently close. At 55 km there is a significant difference in the estimates, most likely related to a strong neutral flow force dragging the particles along with the flow rather than colliding with the middle plate the middle plate. The detection efficiency of positive particles is also lower than the neutrals and negative, due to the particles having small enough radii to be deflected by the shielding potential on GT1, this is the case for both 55 and 60 km. At 85 km, negative particles bellow with radius bellow 0.8 are attracted to GT1, while the positive follow the air flow.

An estimation of the effective cross section σ_{eff} has also been made, using the MSP density distribution estimated by Baumann et al. (2015) in equation 4.23. The difference in detection efficiency resulting in a significant difference in estimated cross section. 60km 30% of the particles hit the middle plate directly, compared to 1% at 85 km. A possible explanation is the concentration of particles with radii above 0.5 nm accounts for $\sim$ 1% of the total concentration of MSPs. The actual effective cross section is most likely somewhere between the two extremes, since some of the particles passing the middle plate can be attracted to the plates if positively charged. Or they could follow the airflow sufficiently close for charge exchange.

The results are consistent with the pre-flight estimates conducted by Pineau (2017), particles at radii of nm size will enter the probe and reach the middle

plate. The detection rate estimated by the new simulation have is much higher than what was estimated, likely due to the actual rocket velocity being 600 ms^{-1}. The amount of particles directly hitting the middle plate is much lower than the amount of particles passing, as a result of the airflow. However, the charging effects of the middle plate are not yet well understood. At higher altitude the effective cross section significantly decreases, as a result of the decrease in airflow and where the shielding effect is more efficient. It should be noted that the simulations are based on a number of assumptions and approximation of the actual physical situation.

5.4   Ion Motion

The nose cone is opened 51 seconds after launch, corresponding to an altitude of ∼ 50 km. At these altitudes the atmosphere is still significantly dense, and there is a high concentration of ions, (refer to Baumann plot). The air flow simulations uses a drag force, only applicable for particles with much higher mass than the neutral atmosphere. This is not the case for ions. In early papers there have been stated that +6.2V should be significant to shield ions and attract electrons. These considerations were made for closed probes, such as DUSTY, and for a polar summer mesosphere instruments, where larger ice particles are present, which are not necessarily singly charged. In addition the rocket had an average velocity of ∼ 1400 at altitudes between 60-90 km. This will result in a strong flow through the probe.

Figure5.7 shows various energy graphs, depending of velocity, and radius. The velocities are based on the rocket velocity range in the altitudes between 50 and 90 km. The red line indicate the different energy levels. If Based on this, atoms and molecules bellow 600 amu does not have enough energy to enter the probe, if GT1 has a bias potential of +10 V. With a payload chargin of -4 v, resulting in a shielding of 6 V, is approaching the mass size limit of ions at ∼ 400 amu (Water ion cluster with sim 15 water molecules). However, this is purely based on their thermal and kinetic energy.
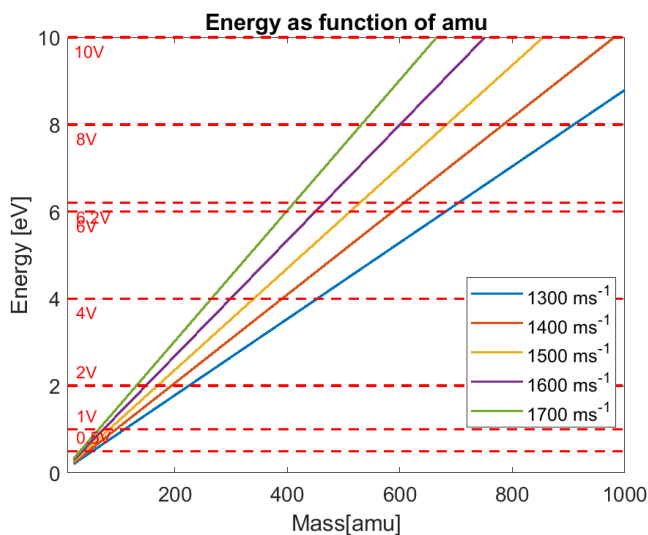

Figure 5.7: Comparison of the shielding energy and the thermal energy as function of mass. Energy is in terms of eV and mass in amu. The plot is made for a range of velocities, from 1300 to 1700 ms^{-1}

(a)

(b)
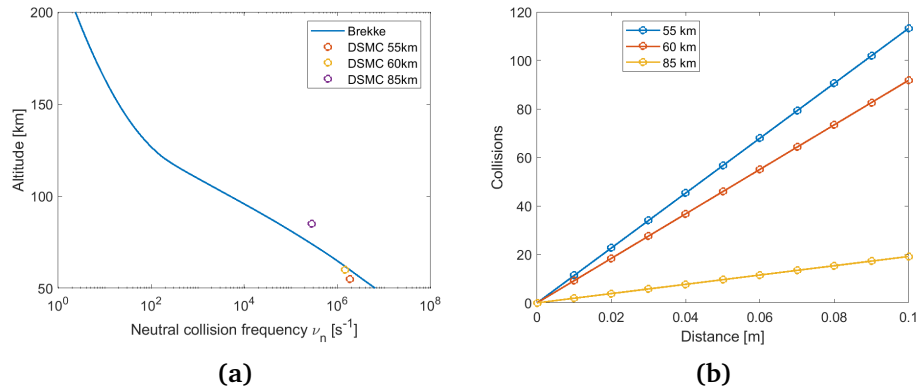
Figure 5.8: (a) Neutral-neutral collision frequency as function of altitude based on equation 5.8a. The neutral density is the from the MSIS model. The collision frequency estimated by the simulations is also plotted for comparison (b) Neutral-neutral collision frequency as function of altitude based on equation 5.8a. The neutral density is the from the MSIS model. The collision frequency estimated by the simulations is also plotted for comparison

The neutral collision frequency, calculated using formula 4.26 and the neutral density from the MSIS model, and the results are plotted in figure 5.8a. For comparison the results of the DSMC simulations are also plotted. There is a good correlation between the simulations and the calculation. Collision frequencies are on the order of $\sim 10^6$. Using the velocity of the rocket, considering this as the relative velocity of the ions, an estimation on the number of collisions can be found. Figure 5.8b show the results for all the three focus altitudes of this thesis. For a distance traveled of 0.03 m, the number of collisions is ~ 30 both for 55 and 60 km. The most abundant species at these altitudes are NO+ with mass are around the mean mass of the neutral gas, ~ 28 amu. Considering the momentum transfer in a completely elastic collision between a neutral moving with the rocket velocity, and an ion at rest, completely deaccelerated by the shielding potential. Assuming that the ion retains all the momentum of the neutral, it would require ~ 30 collisions for the ion to gain enough energy to enter the probe. This suggest that there is high probability that the ions will enter the probe. In the future, the ion motion should be accounted for in a more precise way, using Brownian motion models.

High energy protons during a solar proton event in a range from 10 to 500 MeV that reach altitudes of 50-60 km (Seppälä et al., 2008). These would have more than enough energy to enter the probe, considering a +10 V grid voltage is 10 eV. During the launch EISCAT observed slight precipitation events, but the solar wind and activity does not suggest a solar proton event. With this knowledge, the probe seems to be unsuitable to measure dust during solar proton events.

This in terms is a contradiction to the chance of PMWE conditions, considering investigation of the occurrence of PMWE suggest they are more likely to happen after a solar proton event.

/6

G-chaser Campaign

In this chapter the details around the rocket campaign will be discussed. Section 1 covers the details around the rocket and payload, information provided by NASA Wallops Flight Facility. The student teams are presented in section 2, with information provided in reviews and personal correspondence. Section 3 presents testing and integration. Section 4 covers the ionospheric conditions during launch and in section 5 the data from the rocket is presented.

6.1   Rocket and payload

The rocket was of a type Terrier-Improved Malamute, developed at NASA Wallops flight facility. It is a two stage spin stabilized rocket. The first stage booster was a surplus military Terrier MK12 and the second stage was an improved Malamute, both boosters had four fins in a cruciform configuration. The payload had a 0.3556 m (14 in) diameter and bulbous 0.4384 m (17.26 inc) diameter, with a cone angle of 11°. The top part of figure 6.1 show the mechanical design of the full rocket, with both boosters and the payload (Sounding Rockets Program Office, 2015).

The payload consisted of four parts. On the bottom deck were most of the student experiments. Next was a telemetry part. On top of that was the 4D-model developed by the university of Oslo and Andøya Space Center. On top was the nosecone, together with SPID a instrument from University of Oslo was

located. Figure 6.1 shows the overall design of the payload of the rocket.
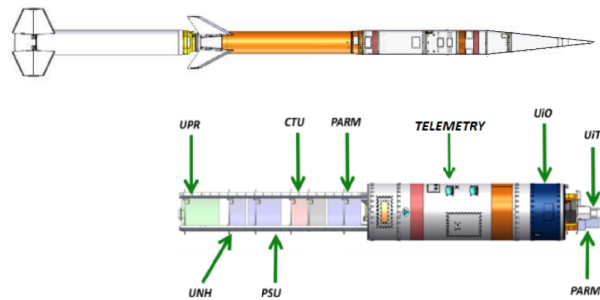
Figure 6.1: Figure showing the rocket and an enhanced view of the payload and student team placement. The abbreviations are listed in section 6.2. By courtesy of Sounding Rockets Program Office (2015)

6.2 Student Teams

In total there were 7 student teams on the G-chaser rocket, with students from Norway, Japan, Puerto Rico and the US. The overall science objectives of the teams were focused on PMWE and pulsating aurora.

University of Oslo (UiO):
The team from the University of Oslo, in cooperation with Andøya Space Center, worked on a 4D module. This consisted of a mother part and daughter probes that was ejected at an altitude of 70 km and established connection with the payload. The daughters were equipped with Langmuir probes of different configuration, aimed at measuring small-scale electron density, that later can be analyzed to study plasma turbulence and instabilities.

University of New Hampshire (UNH):
The University of New Hampshire team had built a lidar designed to observe Nitric Oxide (NO) air afterglow emissions directly vs. altitude. The data would be analyzed to calculated NO densities and enhancement to be compared with typical background values.

University of Tokyo (PARM):
With two instruments onboard, the PARM team focused on pulsating aurora. One of the instruments were a particle detector to detect incoming pulsating aurora electrons. They measured in a wide energy range from a few tens of keV to a few MeV. The second instrument was an optical instrument, designed

to study the temporal and spatial variations of pulsating aurora, located in the nose cone next to SPID.

Pennsylvania State University (PSU):
With an onboard lidar, the team from PSU wanted to take measurement of the PMWE, to contribute to the understanding of formation processes of PMWE. They wanted to use both rocket born instruments and compare to ground measurements during the campaign.

University of Puerto Rico (UPR):
The student team from Puerto Rico University did a UV-VIS-NIR Emission Spectroscopy, aimed to observe pulsating aurora. They also expected to obtain data of pressure and temperature from the rocket trajectory.

There was an overall agreement with most of the instrument, but the detailed scientific method was very different. The launch was a success, but some of the other student teams experienced problems with their systems.

6.3   Scientific conditions during launch

G-chaser is a student rocket initiated as a collaboration between NASA Wallops ight facility and Andøya space center. G-chaser is part of the grand challenge initiative, comprised of seven internationally organized rocket launches, aimed at studying the polar cusp region. The G-chaser rocket was launched from Andøya Space Center at 69.29 ° N, 16.02 ° E. Launch time was 09:13:00 UTC, with an azimuth angle of 5.8° and elevation of 82.8 °. The launch was a success with ballistic impact $\sim$ t+5 min after launch.

During the G-Chaser campaign, radar observations were made with the MAARSY 53.5 MHz radar located close to the launch site (69.30° N, 16.04° E) (Latteck et al., 2010). Observations were also made with the EISCAT VHF and UHF radars in Ramfjordmoen (69.35° N 19.13 ° E) at 224 MHz and 930 MHz, respectively (Folkestad et al., 1983). MAARSY provides sensitive observations of PMWE. EISCAT observes PMWE less frequently but provides incoherent scatter data that contain information about ionospheric conditions, see chapter 2. The ionospheric conditions during the campaign are summarized below.

Table 6.1: Details on the UHF arc1 and VHF manda experiments that was used during the campaign.

Dsp exp	Pulses [μs]	Sampling [μs]	Resolution [km]	Ranges [km]	Time resolution [s]
arc1	64x6 AC	6	0.9	96-422	0.44
manda	61x2.4 AC	1.2	0.18-0.36	19-209	5

Figure 6.2 shows the UHF electron density measurements from the launch day (13.01.19). The program started at 05:00 UTC and ended at 12:00 UTC. The radar had an azimuth direction of 290° and 35° elevation, which is in the direction of the predicted trajectory. The arc1 program was running, with a height resolution of $96 - 422$ km, more details in table 6.1. Weak electron precipitation can be seen all the way down to ~ 90 km, suggesting auroral conditions.

Figure 6.3 shows the electron density measurements done by the VHF during launch. The program started at 02:00 and ended at 12:00 UTC. The VHF was pointing in a vertical direction. There was weak electron precipitation down to $\sim 90 km$ at time of the launch, with electron densities on the order of 10^{10}. Both the VHF and UHF show increasing photoionization of the F region. Neither the VHF or the UHF show signs of PMWE. PMWE usually have spatial scales longer than the Bragg scale of the VHF and UHF, which for the VHF is ~ 0.67 m and for the UHF ~ 0.16 m.
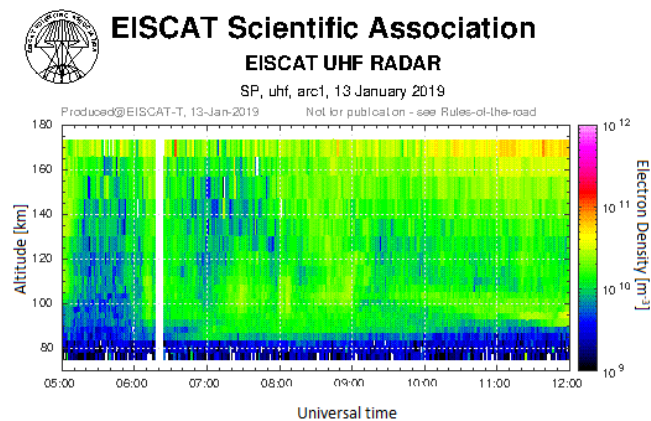
Figure 6.2: EISCAT UHF electron density [m^{-3}] between 05:00-12:00 UTC on the launch day. Antenna was pointing in the direction of the rocket trajectory. By courtesy of EISCAT scientific association
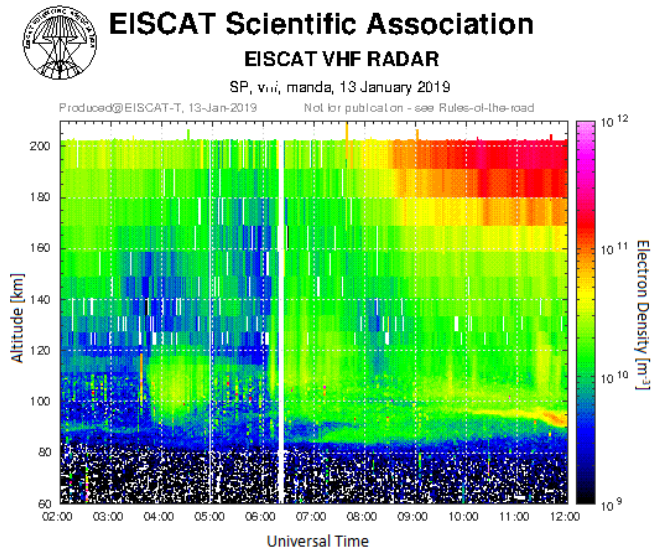
Figure 6.3: EISCAT VHF electron density [m^{-3}] between 02:00-12:00 UTC on the launch day. The antenna pointing in a vertical direction. By courtesy of EISCAT scientific association
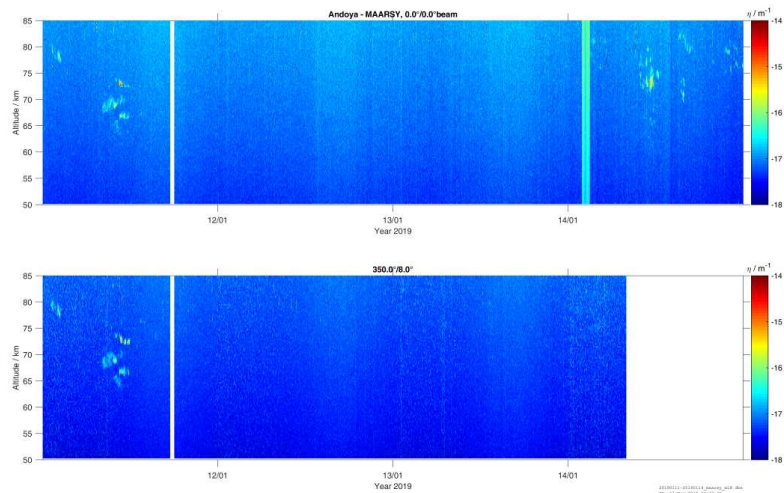
Figure 6.4: MAARSY observation from 11.01.19-14.01.19 starts and ends at midnight. The top plot shows the PSD with beams pointing in a vertical direction. The bottom plot show the PSD in the predicted trajectory of the rocket. By courtesy of R.Latteck IAP Kühlungsborn

Figure 6.4 show the MAARSY observations during from 11.01.19 -14.01.19. The 11.01.19, around noon there where three clear PMWE layers in the altitudes between 65 and 75 km. The following two days, including the day of the launch, the conditions are very quiet. The day after the launch, 14.01.19, there are several weak layers around noon, located at altitudes around 75 km. The top plot show the vertical beam and the bottom plot show the beam pointing in the predicted trajectory, a few degree of the final launch settings. Had the beam been pointing in the rocket trajectory, there would have been a strong signal due to the reflection of the rocket.

Magnetometers were also observed during the launch. The NASA satellites ACE and Discovery showed weak solar wind speeds, and weak southward B_z component. The ground magnetometers showed weak variations in the local currents.

6.4   Rocket data

With a nominal altitude the rocket was expected to reach an apogee of 173.9 km, the actual apogee was at 184.1 km, almost two sigmas higher than expected. Figure 6.5 show the trajectory and total velocity of the rocket with respect to time. Time is in seconds after launch. The average velocity of the rocket on the upleg to apogee, after nosecone separation was ~ 1400 ms^{-1}. At apogee the rocket had a minimum absolute velocity of $427.5 ms^{-1}$
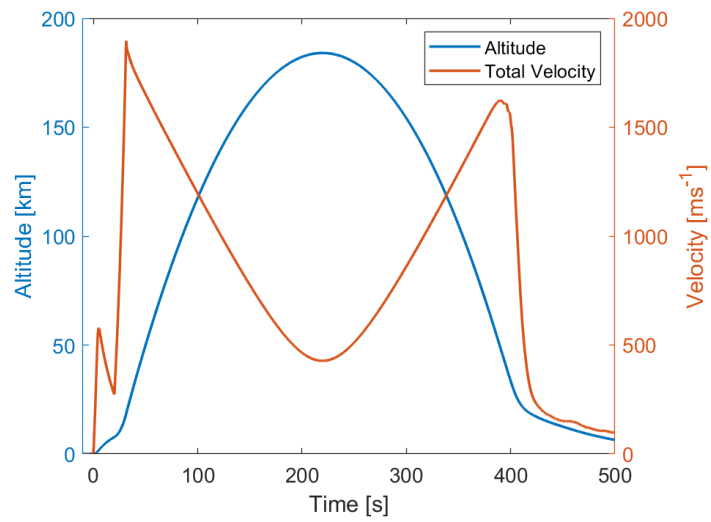
Figure 6.5: Altitude and total velocity of the rocket. Blue line indicated the altitude in km, corresponding to the left yaxis. The orange line is the total velocity in ms^{-1}, corresponding to the right yaxis. By courtesy of NASA Wallops Flight Facillity
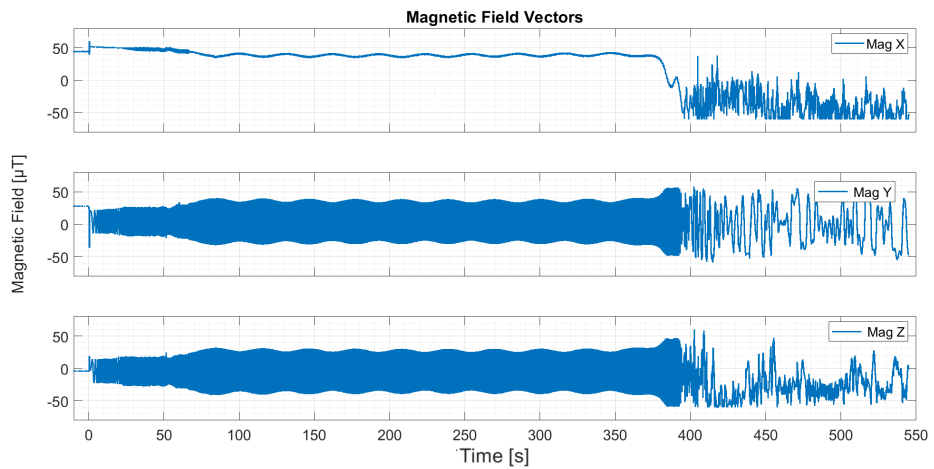
(a)
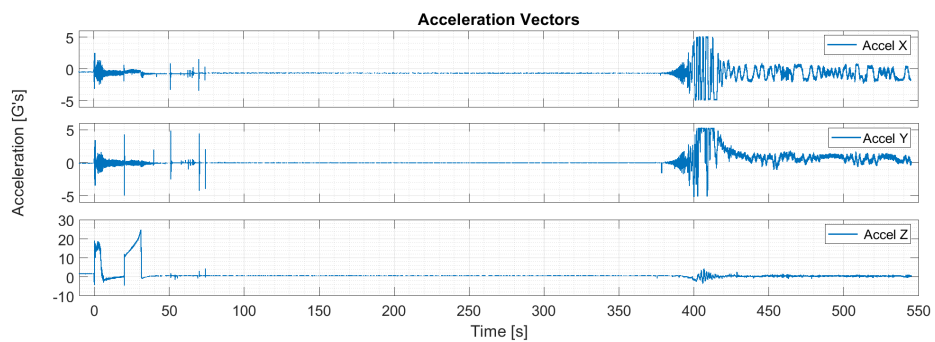
(b)

Figure 6.6: (a) Magnetometer vectors from rocket, where the x component is pointing
along the symmetry axis of the rocket. Units are in micro Tesla and time
is in seconds after launch. Precession effects can be seen clearly as the
sinusoidal motion. (b) Acceleration vectors from rocket, where Z is in the
direction of the symmetry axis of the rocket, units in G's. No clear spin
component, but clear spikes at ∼ 50 to 80 seconds can be seen, in addition
to the two stage burn-outs the beginning of the z vector. By courtesy of
NASA Wallops Flight Facillity

Figure 6.6a show the magnetic vectors in μT as a function of time after launch.
Prior to the despin at ∼ 60s the signal has a clear spin component without
precession effects. After the despin, precession affects become stronger. The
magnetometer gives information on the attitude of the rocket, but for this thesis
these considerations have not been made.

Figure 6.6b show the acceleration vectors in G's as a function of time after launch. Z component along the symmetry axis of the rocket. Can clearly see the acceleration due to the first and second stage. Several spikes occur between 50-80 s, that corresponds to timer events, more in detail in the next chapter.

Figure 6.7 show the raw currents form SPID, as function of nA and seconds after launch. The currents are plotted corresponding to placement position in the instrument. The nosecone was separated 51 sek after launch. The two top grids became saturated quickly after being exposed to the surrounding atmosphere, due to a miscalculation of the pre-amplification settings. The middle plate measures a strong signal right after the nosecone separation, followed by a very quite period. Then the signal picks up in the region from 54 to 57 seconds, suggesting a layer of particles. The next interesting part is in the region between 80 and 85 seconds. All three bottom grids show clear rotational effect. Another striking effect on the middle plate signal, weakly apparent in the current on GB1 as well, is the parabolic shape of the measured current. The signal and effects will be analyzed in the following chapter.
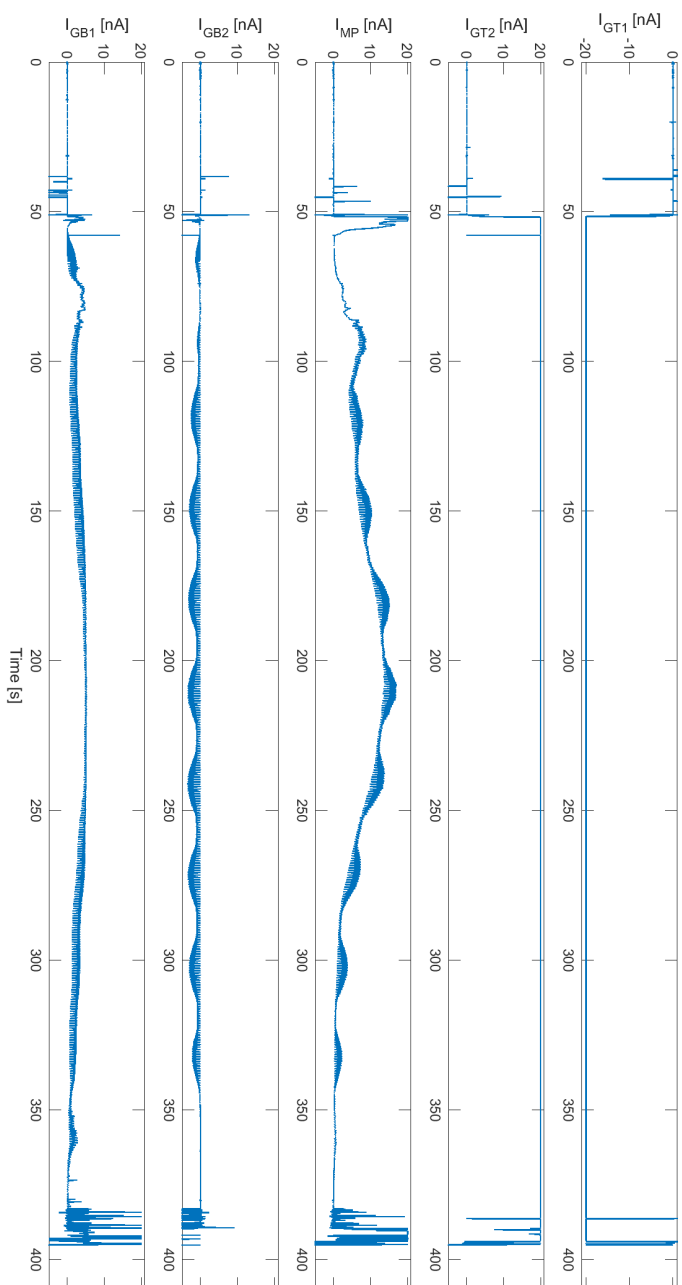
Figure 6.7: Raw current from SPID from launch t = 0 to loss of signal at t = 395 s. The currents are plotted corresponding to the grid placement, i.e top figure is the GT1 grid and the bottom plot is GB1. Currents are in nA and time is in seconds after launch.

/7

Data analysis

This chapter consist of two parts. The first part is considering how external factors influence the signal, such as rotation and action events such as payload separation. After identifying the effects and regions of external events, a spectral analysis, including fft, wavelet analysis and Power spectral densities is presented. In the last chapter the simulation results from chapter 5 and the results from the spectral analysis are combined to derive estimations for number densities.

7.1   Influence of timing events on measurements

Timer events in a rocket campaigns refers to all times when an action has to be made. These actions can be turning on instruments, or actions regarding separation of elements on the rocket. Due to the sensitivity and design of the middle plate grid of SPID, some of these signals can be seen in the observed data. Only the timer events in the times between 51 and 90 s, corresponding to ~ 50-100 km is considered. This region is in the altitude range of interest, where MPSs typically exist. Figure 7.2 show the three bottom grids and the timerevents indicated by the red line. Table 7.1 lists the timer events considered and their abbreviation seen in the figures.

In the previous chapter the accelerometer data was presented, where spikes are seen corresponding to the timer events listed. A closer view of the y component

Table 7.1: Timer events were time is in seconds after launch.

Time [s]	Event	Abbreviation
+ 0	Launch	
+ 51	Nosecone separation	NC
+ 68	UiO Deploy doors	UDO
+ 60	UiO deploy payloads	UDD
+ 66	Despin	DS
+ 70	Payload separation	PS
+ 74	Aft skirt separation	ASS

of the acceleromter can be seen in figure 7.1, where the red lines indicate the timer events, and abbreviations can be found in figure7.1. The magnetometer is not effected by most of the timer events, which can be seen in figure 6.6a, except for the despin.
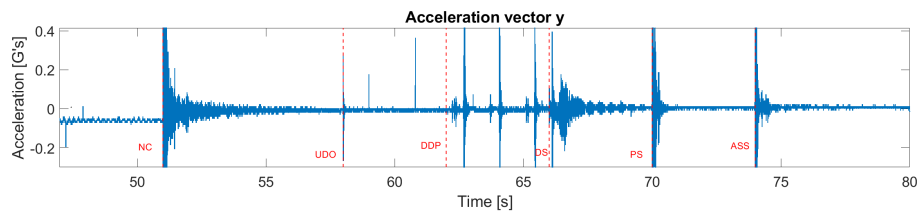
Figure 7.1: Acceleration y vector from 47 to 90 sek. Timer events are indicated by red dashed line. For abbreviations see7.1
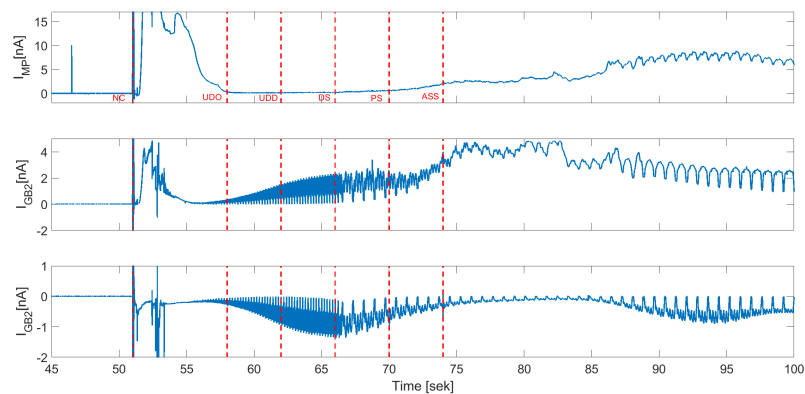
Figure 7.2: Figure showing the raw signal of the three bottom grids. The red lines indicate timer events.

7.1.1 Nosecone separation

To expose the instruments located in the nosecone, such as SPID, to the outside environment, the nosecone is separated at a suitable altitude. In the case for G-chaser, the nosecone separation took place 51 sec after the launch. The middle plate of SPID, as discussed in chapter 4, consist of seven solid sensitive concentric rings. Even small vibrations on the payload will cause a current on the grid, usually propagating as short lasted high frequent symmetric oscillations. The nosecone separation involves a charge being deployed, resulting in vibration of the payload. Figure 7.3 shows the MP signal and what it looks like before and after the nosecone is separated, red line indicating the nosecone separation. The enhanced current could also be generated by residue from the separation, which explains the non-symmetric form of the signal.
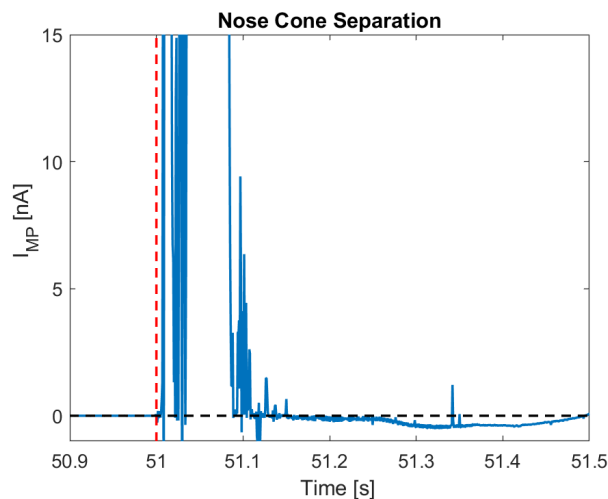
Figure 7.3: Raw data zoomed for the nose cone separation. Red vertical line indicating 51 sec after launch when the nosecone was fired.

Milliseconds after the squib releasing the nosecone is fired, the signal increases significantly and becomes saturated. The signal is the result of vibrations as a consequence of the squib. In addition some of the signal could be the result of powder residue interacting with the middle plate. 0.1 seconds after the squib has been fired the signal is significantly decreased.

7.1.2 UiO doors

58 seconds after launch the doors of the UiO instrument were deployed. The acceleration vector, figure 7.1, shows a clear spike at that time. Figure 7.4 show

the middle plate current, where the red line indicates the door deployment. There is no clear vibrations change in the current. Right before and right after there is a decrease, and then an increase in the signal respectively. This will not be investigated further at this point.
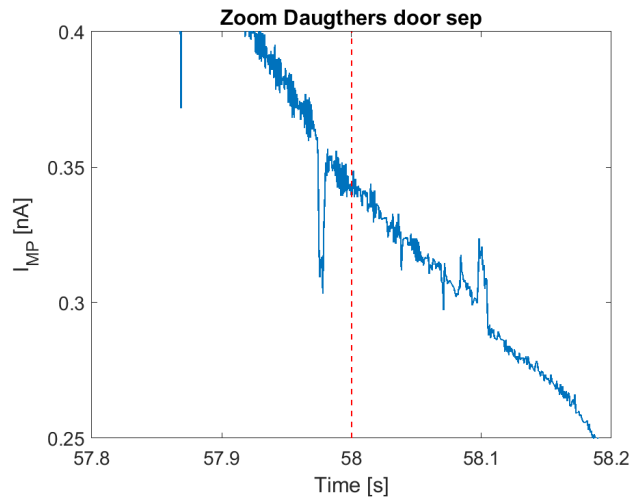
Figure 7.4: Close up of time when the UiO 4D module doors where separated. Red vertical line indicating 51 sec after launch when the nosecone was fired.

7.1.3   Despin

For some experiments, the spin of the rocket can be a problem. Certain experiments favor a lower spin of the rocket, which will result in more samples per volume. When the rocket reaches a desirable altitude, the despin is activated and the spin is slowed down. The spin is not completely stopped, in order to maintain a stability and keep to the trajectory. Figure 7.5 show the MP signal at time of the despin. The signal gradually changes frequency component. The rotational effects will be further discussed in the following sections.
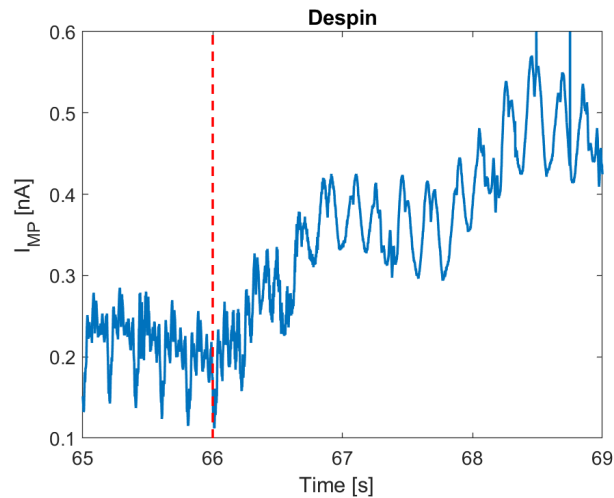
Figure 7.5: Raw data zoomed for the despin. Red vertical line indicating 66 sec after launch when the despin was activated.

7.1.4 Payload and aft skirt separation

Figure 7.6 show the times when the payload (a) and the aft ski(b) were separated, exposing all of the instruments to the atmosphere, for placement see figure 6.1. These effects both manifest as standard vibration effects, i.e the signal is enhanced on both sides of the background signal, and very high frequent oscillations can be seen. The time duration of the effect is on the order of 0.1 sek, and therefore has little implication on the overall signal.

Timer events effect the middle plate signal in different ways. The purely vibrational effects, like the payload and aft skirt separation, appear as vibrations in the signal. The nosecone separation results in a significantly increased current, combined with vibration. This could be the result of residue from the separation. The despin effects the entire signal, in that sense that it changes the already existing frequency. The timer events located within the altitudes of interest ($\sim$ 50-90 km), are the nosecone separation and despin. To avoid the corruption of the signal analysis, the altitude regions prior and including the nosecone separation is not included in the rest of the analysis.

Figure 7.6: (a) Detail of the payload separation effect on the signal. Red line indicating time of payload separation. (b) Detail of aft skirt separation effect on the raw signal. Red line indicating time of skrift separation

7.2   Background current

In this section the background current is considered, which referrers to the smooth slope the measured signal seemingly follow to apogee. Background currents have been observed in many rocket experiments over the years (Surdal et al. (2009), Havnes et al. (2018), Smiley et al. (2003), Brattli et al. (2006)). There are several theories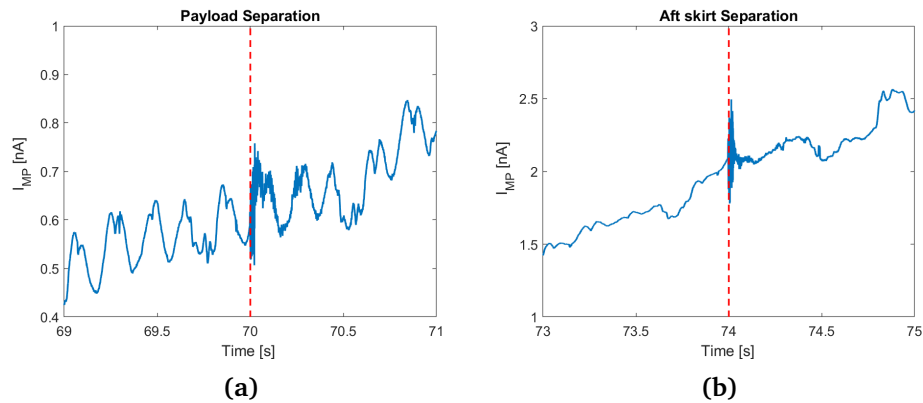 on why such currents are observed, some regarding plasma leakage current, others on payload charging, but there is yet to be a clear understanding of it. The background current usually follow a smooth curve, increasing with altitude. The rocket altitude and current on MP are both shown in figure 7.7. The red line indicates the apogee of the rocket trajectory. There is a correlation, between the current and altitude, but the peak of the signal does not appear to be exactly at apogee. Since the background follow a smooth curve, both on the upleg and downleg, it does not suggest to be the result of incoming particles. The rocket did not have attitude control, and is therefor mostly shielded from the airflow on the downleg.

To better see the underlying variations of the signal, one way is to make a fit of the graph and subtract it from the signal. Several considerations must be made prior to making the fit. Areas where the signal seemingly deviates from the background current, will shift the fit of the signal. For this reason the times from 53 to 64 sek, including the noise of the nosecone separation, and the following layer where the signal shows a strong current of $\sim$ 17 nm. The other region where the signal deviates from the background between 80-130 seconds are also cut out. The resulting graph is shown in figure 7.8.
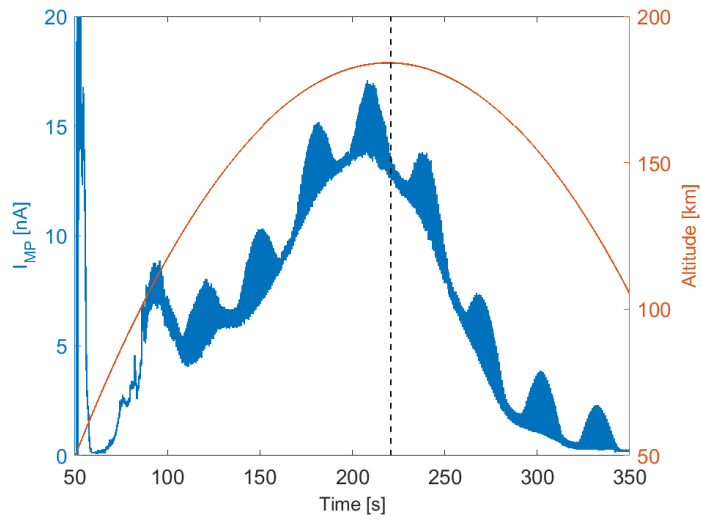
Figure 7.7: Middle plate current from 50-300 sek.

The altitude range of interest in this campaign is the altitudes between ~ 50 to 90 km. This corresponds to the time range ~ 55 to 130 sec. The removed parts are within this time range, which leaves a relatively small portion of the signal on the lower part of the upleg contributing to the fit.
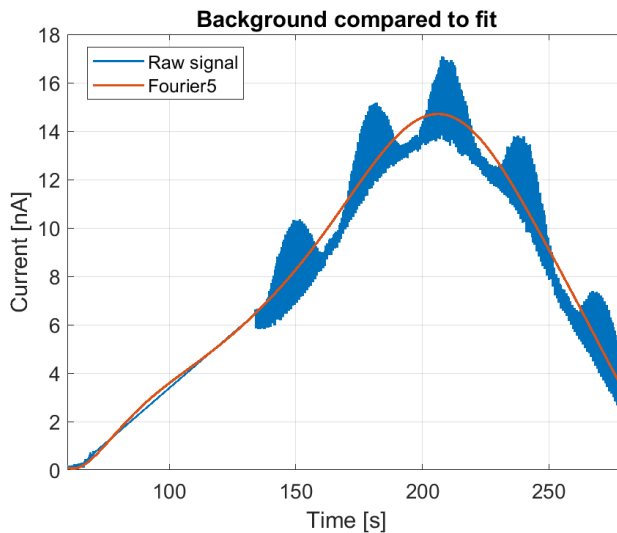
Figure 7.8: Raw signal without dust layers fitted to a 5th order fourier graph

Deciding which fit is the best depends on a range of factors. In this case, the best fit was decided by how well it correlated with the lower altitude signal patch, with an overall R-squared value of 0.9629. The background subtracted current is shown in figure 7.9. The signal is concentrated around zero.
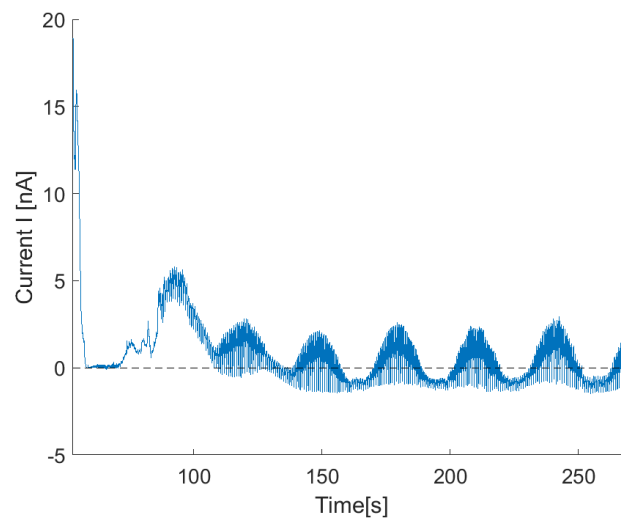
Figure 7.9: Background subtracted current. Shows that the signal is oscillating between positive and negative. The mean of the current is 0.0722 nA.

The time is converted to altitude and figure 7.10 show a zoomed view of the lower altitude current. The two clear layers of enhanced current is in the altitude range of 55 to 60 km and 85 to 100 km. Between these two altitudes the signal almost drop to zero. This suggest that the measured current is possibly the result of particles existing in stratified regions. MSPs have been proven to do so, based on the research related to summer experiments and PMSE (Antonsen and Havnes, 2015).

Another clear effect on the signal is the periodic motion of it, especially clear in higher altitudes. These effects will be discussed in the following section.
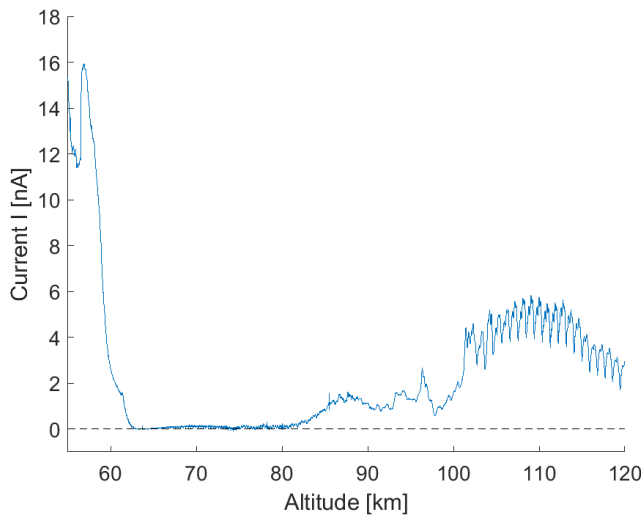
Figure 7.10: A zoomed view of the background fit for the lower altitudes. Note that the x axis now is in terms of altitude [km].

Since the fit is made based on a small part, compared to the rest of the signal, for the spectral analysis, the raw current is used. The cause for the background current is also not known, thus removing it, could potentially remove significant information in the signal.

7.3   Spectral properties

In the previous section the background effects was considered, but not accounted for due to the uncertainties. However, it is clear from the current on the middle plate that for altitudes above 110 km, the signal is governed by periodic motion, in addition to the steady background increase. This section will investigate the rotational and spectral properties, that will give information of the signals shape and spatial dependence. In this section four approaches are used. Considerations of the precession of the rocket will be discussed first followed by a Fast Fourier Transform (FFT) to see local frequency components.The global trends and altitude dependence of the signal are considered using a Wavelet Transform. The small scale trends and wavenumber dependence of the signal is found using a Welch Power Spectrum Density.

7.3.1 Precision

When the rocket spin is decreased by the despin, the motion is more probed to torques. As a result the rockets will begin to rotate around a vertical axis. This effect can be seen in all three bottom grid signal, see figure 7.10. The magnetometer data is compared to the middle plate current in figure 7.11. Both showing a coning frequency of $\sim 0.032Hz$. The figure show the three magnetometer components in μT, x pointing along the rocket axis of symmetry. Current in units of nA. Red line is indicating maximum positive amplitude of the x component, corresponding to minimum for the y and z components. The MP signal appears to have a small phase shift from the magnetometer data. This suggest that peak amplitude for SPID is not correspondent to the alignment of the magnetic field component. Another feature that is clear from the figure is the smoothness of the magnetometer data compared to the grid currents. As a result of SPID measuring particle flux, whereas the magnetometer measure the magnetic fields, unaffected by the outside environment.
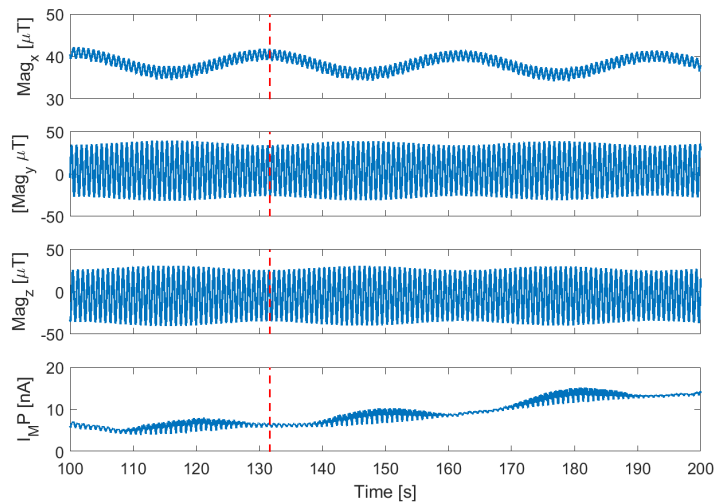
Figure 7.11: Comparison of the magnetometer data and the middle plate current. Axis description of magnetometer can be found in chapter 6. Red line indicating maximum amplitude of the x component magnetometer data.

7.3.2 Fast Fourier Transform

To investigate the frequency components of three bottom grid signals, Fast Fourier Transform is applied to local regions, details on the method can be found in section 4.7. Four regions are considered all of 3 km span, identified from the enhanced regions in the middle plate current 7.10. 3 km is chosen

to have sufficient amount of periods to see the frequency component. Later when looking at the power spectrum, shorter altitude regions are considered to consider the small scale trends in the signal. Region 1 is the altitude between 56 to 59 km, showing a strong current on the order of $\sim 17nA$ shortly after the nosecone is separated. Region 2 is a calm region at 63-66 km, close to region 1, for comparison. Region 3 is the region between 95 to 98 km, a region where the signal deviates from the periodic background current. Region 4 is for comparison of region 3 at altitudes from 109 to 112, where the signal follow the periodic

Region 1, between $56-59$km show a significantly enhanced current, lasting for several kilometres. This region is of particular interest, due to its signal shape, strength and location in the lower layer of the mesosphere, right in the limit to where PMWE occur and large dust particles exist. Figure 7.12 show the three bottom grid signals and their fft. Figure (a) show the normalized fft spectrum with a frequency range of 1 to 40 Hz. The MP spectrum has no clear frequency components. GB2 have several peaks, first at $f = 3.523$, however this is not the rocket spin frequency. From the magnetometer the rocker spin freq is f = 5.20, corresponding to the next peak. The following peaks correspond to the harmonics of the spin frequency. The spectra for GB1 does not appear to have a clear rocket spin component, but the second to fourth harmonics. Note that the y axis is different for all three grids. Figure (b) show the local current. The signal shape correspond well with the fourier transform. GT1 has a peak corresponding to the peak on MP. Should be noted that both these grid have negative bias potentials, and should attract positive particles. To compare the results of this region to that of a quiet region another fft is done for the altitude rage 63-66 km.

Figure 7.13 show the fft and local current for region 2. For all three grid the fft show corresponding frequency components consistent with the rocket spin frequency of $f = 5.28Hz$, and its harmonics. The rocket spin usually vary a little, as is seen. Compared to region 1 all three signals show similar shape. The middle plate show less rotational effect than the two bottom grids. In addition the middle plate current is now ~ 0.15, two orders of magnitude lower than from the previous region. Grids have cross sections of ~ 0.02 compared to the middle plate. In this region however, the two bottom grids measure a much higher current than the middle plate.

(a)

(b)

Figure 7.12: Comparison of fft and currents on the three bottom grids from 56.5 to 59 km (a) Normalized spectrum from fft. Note that the y axis for each grid are different (b) Local current in nA as function of altitude.

(a)

(b)
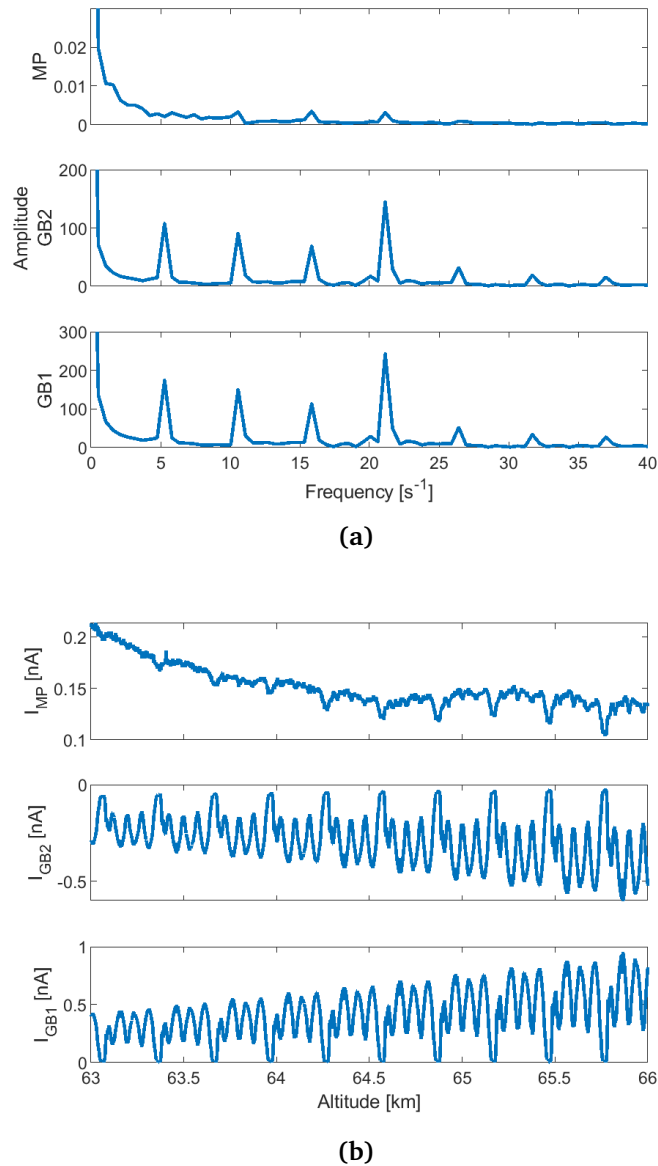
Figure 7.13: Comparison of fft and currents on the three bottom grids from 63 to 66 km (a) Normalized spectrum from fft. Note that the y axis for each grid are different (b) Local current in nA as function of altitude.

The current and fft results from region 3 are shown in figure 7.14. This regions, similar to region 1 show clear differences in the currents. MP and GB1 show a clear increase in the signal. While GB2 show little change from the periodic motion. Region 2 is located some time after the despin, and from the magne-

tometer data the rocket spin frequency is $f = 1.35Hz$. GB2 have frequency components of the spin frequency and several of the harmonics. MP and GT1 show a spin component of $f = 2.25Hz$. This is not an harmonic of the rocket spin. Region 3 is at the limit to where MSPs exist, and at these altitude the larges concentration is of neutrals, unlikely to explain the current. The positive ion concentrations are as high as 10^{10} m^{-3}.

To compare the measurements of this region to that of a quiet region, figure 7.15 show fft and currents from region 4 between 109 to 112 km. All three fft show similar frequency components consisting of the rocket spin of $f = 1.23Hz$ followed by harmonics. The amplitudes of each frequency component varies, MP and GB1 having corresponding minimum points where GB1 have a maximum point.

(a)

(b)
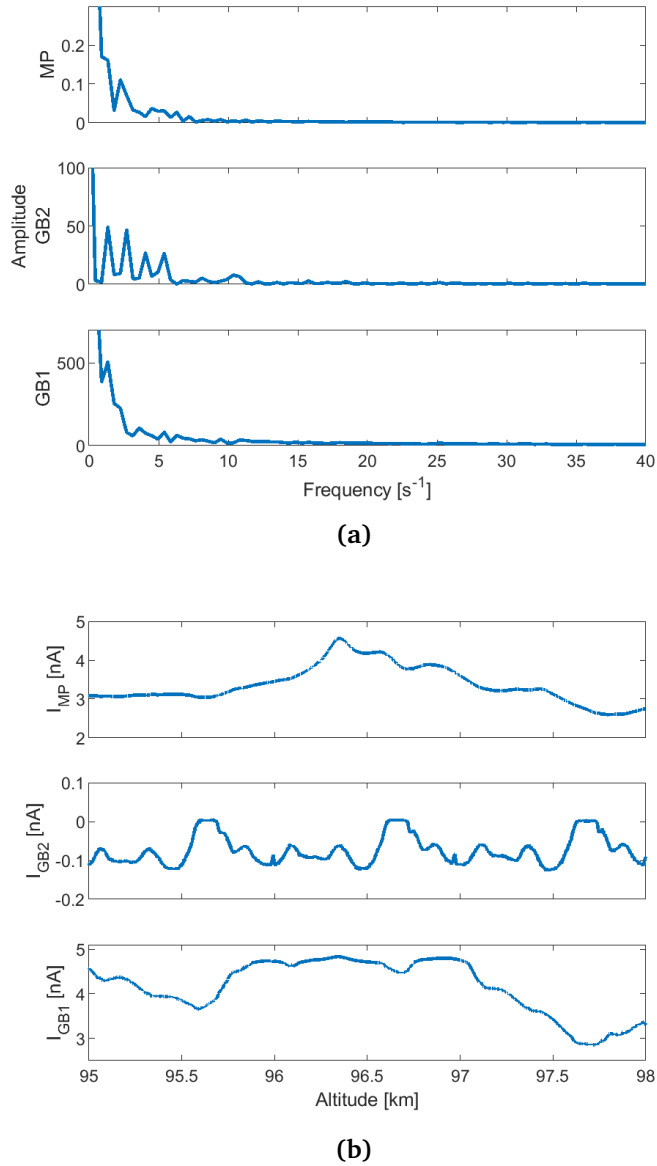
Figure 7.14: Comparison of fft and currents on the three bottom grids from 95 to 98 km (a) Normalized spectrum from fft. Note that the y axis for each grid are different (b) Local current in nA as function of altitude.
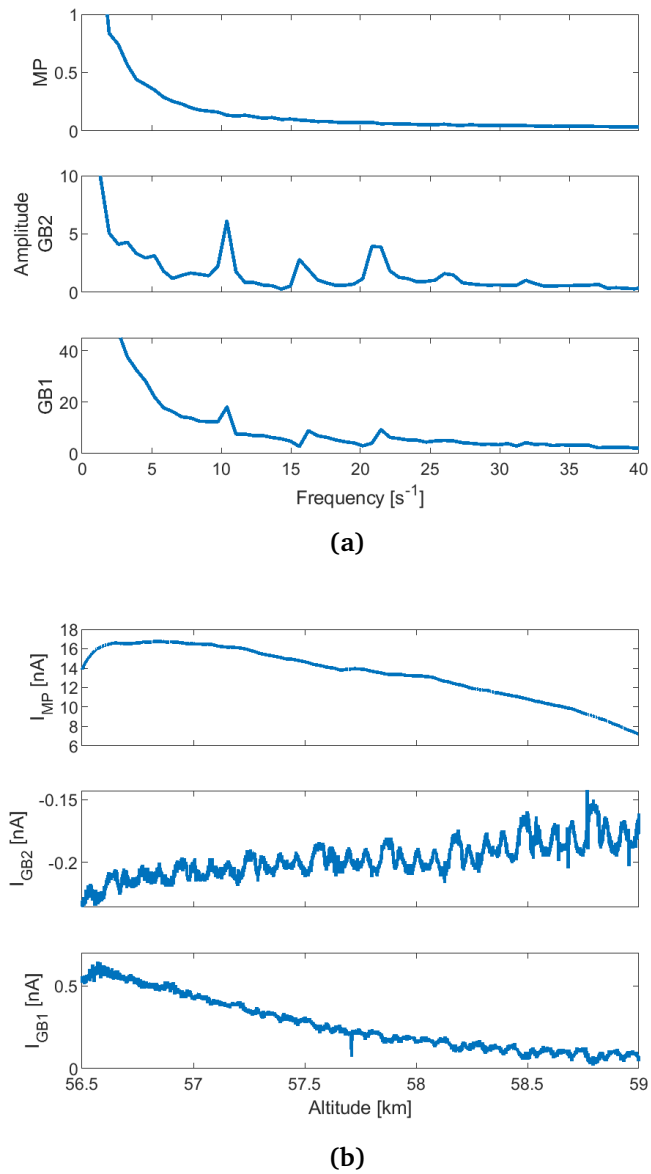
(a)

(b)
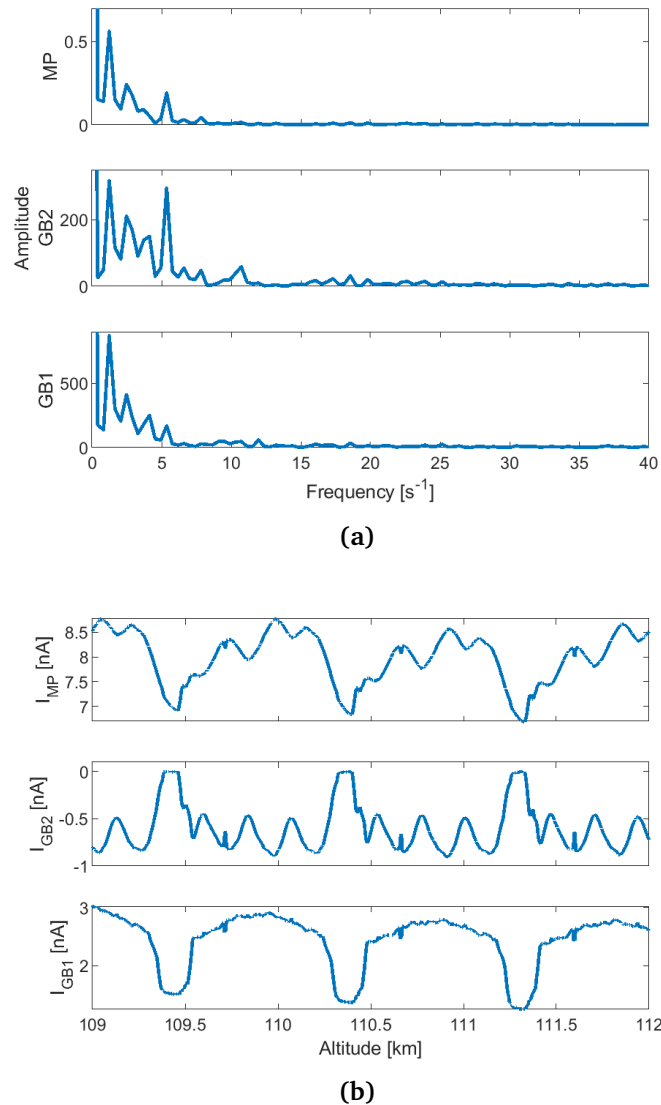
Figure 7.15: Comparison of fft and currents on the three bottom grids from 109 to 112 km (a) Normalized spectrum from fft. Note that the y axis for each grid are different (b) Local current in nA as function of altitude.

After having looked into four different regions, two located prior to the despin there are similarities between the enhanced regions versus the calm regions. There is a clear connection between what is measured on MP and GB1. This could be related to both having negative bias potential and thus both would attract positive particles. If ions were to enter the probe, they could explain the current. However, this would mean that the ions appeared in layered region,

consider the strong increase at ∼ 56 km, and then a drop to ∼ 0.15. MSPs could also explain the correlation of the MP and GB1 current measurement. Simulations of MSP concentration, see section 2.2.2, show that at lower altitudes the majority of the particles are either positively or neutrally charged. Secondary charging could charge the neutral MSPs resulting in a positive current on the middle plate. Not all particles hit the middle plate, as is discussed in chapter 5, and thus some would pas the middle plate and hit GB1. GB2 shows little change in current in the enhanced regions, which argues against the secondary charging effect. If the particles undergo secondary charging, the particles would carry a negative charge from the middle plate. This should suggest that an effect should be seen in the GB2 current, it being positively biased. The particles lose momentum while traveling thorough the top part of the probe. However, after passing the middle plate, they are accelerated.

Another striking feature from the fft results are that in some area MP and GT1 show frequency components not corresponding to the rocket spin. This is the case for higher altitudes, where the precession frequency is ∼ 0.032 Hz. When precession and spin are present in a rocket, it alters the signal, and result in complicated rotational effects. In the higher altitudes where the rotational effects govern the signal a chirp like motion can be seen in the raw current 6.7. This is the result of several harmonics and the coning of the rocket, combined with the small changes in the rocket spin. Why such clear rotational motion occur have not been investigated here. A possible cause could be the result of direct sunlight hitting the middle plate and grids. When the rocket is rotating, the area inside the probe exposed to sunlight varies. This however would need not be investigated further.

7.3.3 Wavelet Analysis

Wavelet analysis contain spectral information both of spatial and altitude scales. Finding the wavelet solution of the signal will show the global variations in the signal. Figure 7.16 show the current as function of altitude and power spectrum from the wavelet for the entire upleg of the flight, as a function of altitude and wavelength. The wavelengths are estimated using $\lambda \sim v_r/f$, v_r is the rocket velocity. The white line in the wavelet spectrum shows the cone of influence in the signal.The global wavelet analysis show that for higher altitudes the signal is dominated by rotational effects from the rocket spins. Several of the harmonics can also be seen. The preseccion of the rocket, the rotational effects result in a chirped signals, as seen in figure 7.11. At the lower altitudes the signal varies greatly. Areas where the signal is not dominated by rotational effects appear as spike in the wavelet. One spike can be seen at ∼ 55 and another at ∼ 95. On the global wavelet it is difficult to see the small scale variations.
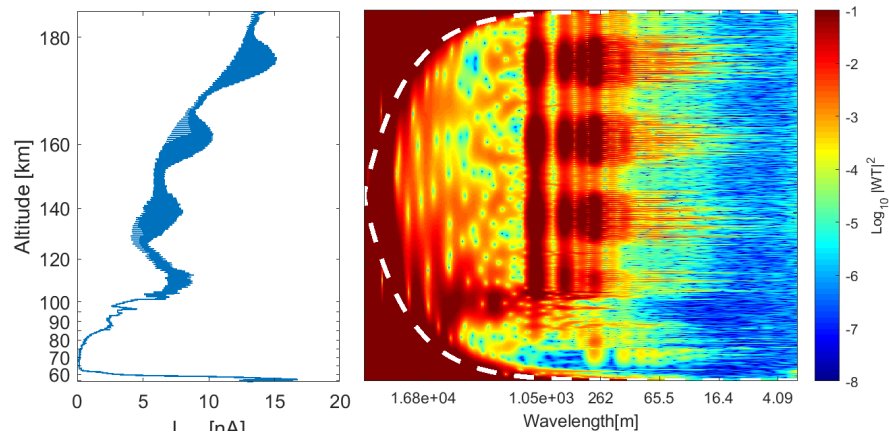
Figure 7.16: Comparison of the middle plate current and the corresponding wavelet spectra from 55 to 183 km. Current in nA and the wavelengths were converted to frequency through $\lambda = v_R / f$.

Figure 7.18 show the comparison of the localized middle plate current and the wavelet spectra from an altitude range of 55 to 64 km. Three spikes are apparent at 55, 56.5, and 61.5 km. One of the spikes are much stronger and stretch down to wavelengths of 16 m. This is much higher than the Bragg scale, consistent with the weak SNR and no PMWE. Another feature that should be mentioned is the trail for low wavelength spikes in two patches. One between 58 to 59.5 km and one at 60.5 to 62.5 km. Looking at the raw current suggest mechanical vibrations of the instrument. It does not correspond to any of the listed timer events. Vibrational effects in the signal appear as high frequent double sided amplitude, also observed in previous experiments (Antonsen, 2019).

Figure 7.17 in the range from 94 to 114 km. The higher parts area show strong rotational effects. In the lower altitudes there is one clear spike in the signal around 96 km. This stretch to wavelengths of 100 m, Another wider spike appear around 102 km, but the strongest part of the signal corresponds to the rocket spin frequency at these altitudes.

The wavelet corresponds with the fft, and additionally show the vertical extent of the signals. The two uppermost region have vertical scales of ~ 2 km. The lowest region is more localized with a vertical extend of ~ 1 km.
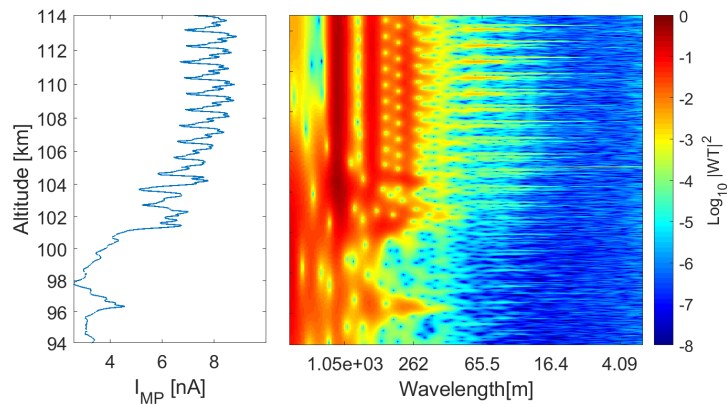
Figure 7.17
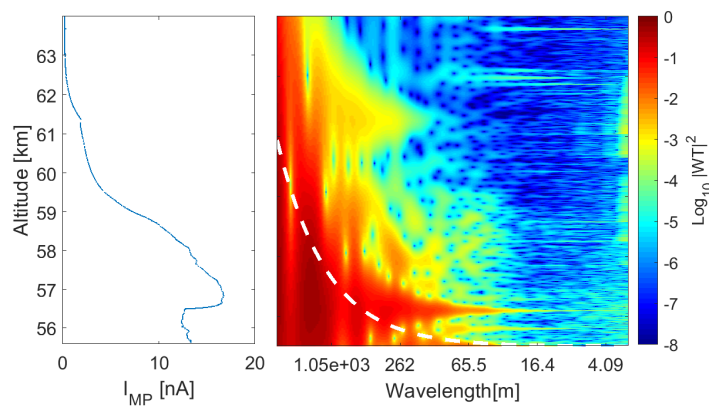
Figure 7.18: Localized comparison of middle plate current and wavelet spectrum in the altitude range of

7.3.4   Power Spectral density

The fft show clear differences between the grids in enhanced regions, while in the calm regions there is good agreement of the frequency components. In chapter 2 the Polar mesospheric winter echoes and their believed driving forces where mentioned. Among these is neutral air turbulence. So called tracers of the turbulence have specific slopes following the wavenumber k corresponding to the motion of the turbulence. By applying a Welch method to find the power spectra density (PSD), the wavenumber dependence of the signal can be found. This method have been applied to several rocket experiment over

the years, including measurements of electrons, ions and MSPs (e.g Alcala et al. (2001); Strelnikov et al. (2003); Brattli et al. (2006); Spicher et al. (2014) and Antonsen et al. (2019)). In this work regions of 1 km, within the regions were the fft was applied are considered. With a sampling frequency of $T_s = 0.0007$, and an average velocity of $\bar{v}_r = 1407 \text{ ms}^{-1}$ in the altitude range $54 - 120$ km, yield 1 sample pr 0.9847 m. However, the lowest spatial scales will be $\sim 2m$, inferring Shannon's sampling theorem. This is just bellow the Bragg scale of MAARSY ($\lambda = 2.8$), which means that the measurements give limited information in the Bragg scale range. On the figures, the Bragg scale is indicated with a black vertical line. Since turbulence in the mesosphere is usually horizontally stratified, see 2, the power spectra is estimated for a range of 1 km. The wavenumber is found using the mean speed of the rocket in the region considered, to account for the correct resolution of the signal. The red line indicate the Kolmogorov spectral slope of $k^{-5/3}$.

As a reference to the noise spectra in the instrument the PSD from 10 to 5 sek prior to launch is shown in figure 7.19. A velocity of ~ 1400, being the mean speed of the rocket between 56 and 110 km is used to convert the frequency to wavenumber. The instrument is not measuring anything but noise from the electronic components. The spectra show that all three grids follow a close to horizontal line, consistent with a typical noise spectra.
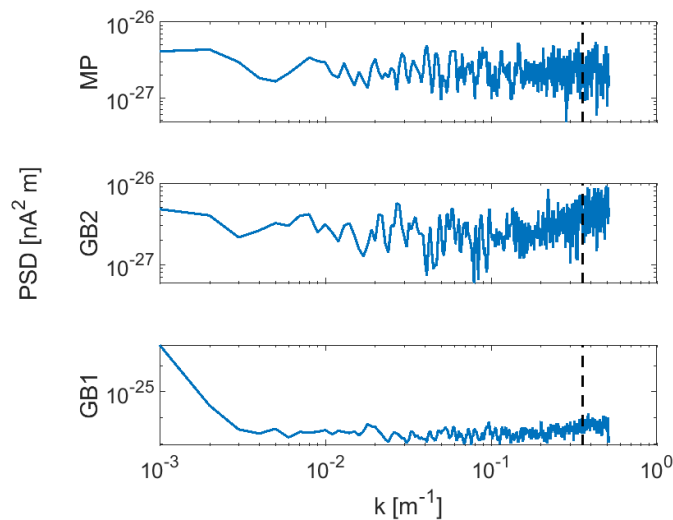
Figure 7.19: PSD prior to launch

Figure 7.20 show the PSD from an altitude range 56.5 to 57.5, within region 1 from the fft section. Clear differences between the three signals was apparent. In addition, the MP current is significantly increased. The PSD of the middle

plate show that the signal follow a spectral slope of $k^{-5/3}$ into the bragg scale, indicating an internal subrange of turbulence. The two bottom grids show signals dominated by noise, consistent with the observed signal and fft showing clean periodic motion.

The second region considered is the wide peak seen in the wavelet spectrum in figure 7.18. The local PSD is shown in figure 7.21. There is a clear frequency component at scales corresponding to the enhancement discussed in relation to the wavelet. In this region all three grids follow the slope. However the two bottom grids have much more noise than the middle plate curve.

The third enhanced region considered is between 96.2 to 97.2 km. The fft showed consistency between the measurements on MP and GB1, and frequency components inconsistent with the rocket spin frequency. The PSD from the three bottom grids are shown in figure 7.22. MP and GB1 follow the $k^{-5/3}$ good. GB2 show a signal more consistent with a noise spectra.

Figure 7.20: Local PSD using the Welch method on the enhanced region at 56.5 to 56.7km . The Kolmogorov slope indicated with the red line and dashed vertical line indicate the bragg scale of MAARSY.

Figure 7.21: Local PSD using the Welch method on the enhanced region at 61 to 62 km. The Kolmogorov slope indicated with the red line and dashed vertical line indicate the bragg scale of MAARSY. The peak close to the bragg scale corresponds to the noise components seen in the wavelet spectrum.

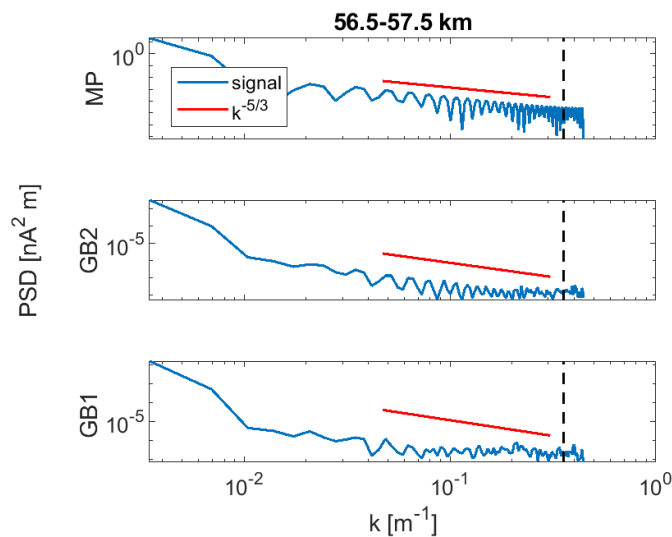**Figure 7.22:** Local PSD using the Welch method on the enhanced region at 96.2 to 97.2 km. The Kolmogorov slope indicated with the red line and dashed vertical line indicate the bragg scale of MAARSY.
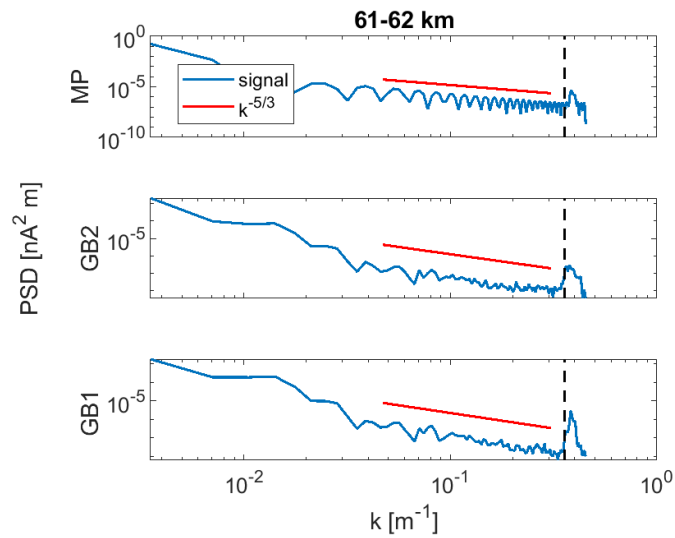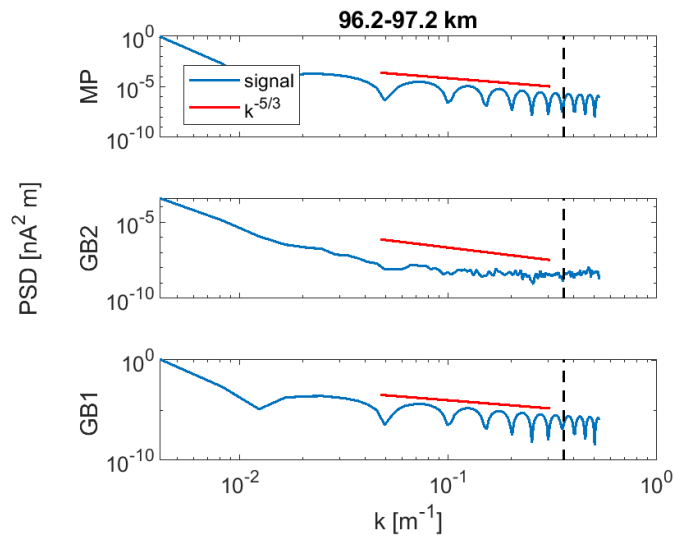
At all three regions where the raw MP current show a strong increase in

signal, the PSD show a wavenumber dependence of $k^{-5/3}$ indicating an inertial subrange of turbulence. The flow is governed by inertial forces, and is referred to an active region of turbulence (Doviak et al., 1993). If the radar bragg scale is located within this region, the turbulence and inhomogenities could be observed. However a radar requires sufficient refractive index, dependent on the electron density. At time of the launch the electron densities where low and could explain why MAARSY did not observe PMWE activity at time of the launch, even though the spectra suggest active turbulent conditions.

There are three distinct enhanced region in the signal. Two of them located in a region where theory suggest dust. The third region is at altitudes of 97 km, well above the region where MSPs exist. This supports the argument that dust can enter the probe. EISCAT observed precipitation down to altitudes of $\sim$ 90 km, increasing the electron densities and ionization. The sampling frequency of SPID limits resolution of the signal. The Bragg length for MAARSY is at the edge of the signal, thus no conclusion can be made regarding the radar conditions. The spectral analysis show that the rocket had a spin of $\sim$ 5 Hz prior and $\sim$ 1.4 Hz after the despin. Regions not dominated by rotational motion, indicate active turbulent conditions with PSD wavenumber dependence of $k^{-5/3}$. Both ions and neutrals can be seen as tracers for turubulence.

7.4 Dust flux

The last consideration that will be made is relating the signal to the simulation and spectral analysis. The dust flux into the probe can be estimated from the measured current following equation 3.1. This estimation is based on the volume of the rocket traverse. The equation requires information on the rocket velocity v_r, the charge efficiency η and the effective cross section σ, in addition to the radius of the probe r_p.

In table 7.2 the calculated number densities (10^{12} m^{-3}) with charge production rates varying from 0.01 to 2 , and effective cross section 0.1 to 1. The current strength set to $I = 17$nA , the velocity to $v_r = 1600$ ms^{-1} and the radius of the probe $r_p = 0.03$m. Number densities required to explain the middle plate current of 17nA are between 10^{10} to 10^{13} m^{-3} . For small values of η and σ_{eff} the number density increases with 10^3, compared to that for large values.

A reference value for η, from estimates done by Tinna Gunnarsdottir and using a dust impact velocity of 400 ms^{-1}, $\eta_{ref} = 1$ for $r_{ref} = 2$ nm. Using equation 4.24 from section 4.5, combined with the size distribution at 60 km from models by Megner et al. (2006) and Baumann et al. (2015), gives an estimation of η

to be ~ 0.6. The results from section 5.3 gives estimates of σ_{eff} at 60 km to be 0.3 when only direct impacts onto the middle plate are considered, and 0.97 with passing and direct impact. The closes estimate to the real situation is somewhere between these. Inferring these consideration, the density is likely to be on the order of 10^{10}m^{-3}.

The estimates derived from model simulations by Baumann et al. (2015), see figure 2.2, show Neutral and positive MSP densities around $\sim 10^8$ for 60 km for September conditions. The variations of MSP number densities seasonal variations and microphysical effects were estimated in a sensitivity study conducted by Megner et al. (2006). They find that MSPs larger than 1 nm are highly affected by the vertical wind in winter conditions, increasing the number density at lower altitudes by a factor of 6 compared to summer conditions. In another model study by Bardeen et al. (2008) they estimate number densities of $\sim 10^9$m^{-3} in December, January and February.

Now looking at the number density estimates in table 7.2, considering that the ions alone could generate the observed current at ~ 60 km. Ions are singly charge, and thus η is 1. If the ions enter, the cross section will likely be high, considering that they will follow the neutral air flow. This yields number density for de ions on the order of $\sim 10^{10}$ to 10^{11} m^{-3}. Simulation for September conditions shows positive and negative ion densities of $\sim 10^9$. Rocket experiments conducted by Brattli et al. (2006) show ion densities around $\sim 10^{10}$ m^{-3} at 60 km, for December.

The number densities observed at ~ 60 km are consistent with some of the model simulations for MSPs. However, model estimations and measurements suggest that ion number densities are of the same order of magnitude at 60 km. The the Kolmogorov slope indicates that the measured quantity is a passive tracer for turbulence, which both MSPs and ions can be. In the future, having an instrument specifically designed for ion densities, and one for the electron densities, together with SPID, determining the number densities.

Table 7.2: Number density (10^{13} m^{-3}) for different α and η for a current of 17nA

		η					
		0.01	0.1	0.5	0.7	1.0	2.0
α	0.1	2.2075	0.2207	0.0441	0.0315	0.0221	0.0110
	0.2	1.1037	0.1104	0.0221	0.0158	0.0110	0.0055
	0.3	0.7358	0.0736	0.0147	0.0105	0.0074	0.0037
	0.4	0.5519	0.0552	0.0110	0.0079	0.0055	0.0028
	0.5	0.4415	0.0441	0.0088	0.0063	0.0044	0.0022
	0.6	0.3679	0.0368	0.0074	0.0053	0.0037	0.0018
	0.7	0.3154	0.0315	0.0063	0.0045	0.0032	0.0016
	0.8	0.2759	0.0276	0.0055	0.0039	0.0028	0.0014
	0.9	0.2453	0.0245	0.0049	0.0035	0.0025	0.0012
	1	0.2207	0.0221	0.0044	0.0032	0.0022	0.0011

8

Conclusion

The main goal of this thesis was to investigate the behaviour of dust particles within the SPID detector and to link it to the observed currents. The focus has been on conditions during the rocket flight around 60 km altitude, where the middle plate detected a strong enhancement. The ion motion and its possible contribution to the measured current were also considered, in addition to timer events. The frequency components governing the current were established by investigating the spectral properties of the signal. The Mach number at 60 km was ~ 5, indicating supersonic speeds. The particle trajectory simulations in the gas flow suggest that at the altitudes of 60 km, particles down to 0.4 should be able to pass the middle plate grid. Particles of this size are on the limit of the model description. Particles of radii larger than 8 nm are efficiently transported through the probe and past the middle plate. The effective cross section, when the dust distribution is considered, is 97% passing the middle plate, and 30 % of those are direct impacts. These values decrease with altitude, as the size distribution of dust particles have a high concentration of sizes < 0.4. In combination with the decrease in rocket velocity and ambient gas density. The simulations also indicate that the rocket shock front is below the instrument, so there is little deflection of the small particles before they reach the instrument. Since the simulation model does not apply to ions, ion motion has been considered by comparing their kinetic energy to the shielding potential, and the neutral collision frequency. Assuming that the neutrals transfer their momentum to stationary ions, through a completely elastic collision, ~ 30 collisions would be required to carry the ions with the flow. With a collision frequency of ~ 40, this suggests that the ions could gain enough energy to

enter the probe. Varying the charge probability and effective cross section at 60 km, estimates number density required to generate a 17nA current to be between 10^{10} and 10^{13} per m^3. The density of positive ions is close to that of MSPs, and so it is also possible that ions cause the measured current or a fraction of it. The spectral analysis show three regions where the signal is not dominated by the rotational effects.

Investigating the relation between MSPs and PMWE was a secondary goal of the campaign. The background atmospheric conditions showed weak precipitation at ~ 85 km, and no observation of PMWE at the launch day. The PSD at 60 km follow the Kolmogorov slope $k^{-5/3}$ to the bragg scale, indicating turbulent conditions. However, the resolution of SPID limits evaluation of the slope around that of the radar bragg scale. This combined with the prerequisite of sufficiently high electron density to observe PMWE, we cannot draw any conclusions on the link between PMWE and MSP from the presented observations.

Based on the work done in this thesis, a number of future works can be suggested to better understand the measurements and to plan future observations. A detailed simulation of the expected dust and ion densities for the mesospheric conditions during the launch could give a better indication of what caused the measured currents. The small scale variation of the signal should also be investigated further. The Fourier transform can be used to filter the signal and show underlying variations that are suppressed by the influence of the payload rotation. In future experiments with probes like SPID, measurements on the electron densities and ion densities should be made simultaneously, to better relate the currents. The design of the probe should be tested in a plasma chamber and an airflow chamber. The transmission of the instrument should be investigated during the design since this might have been too high for the flow regime of the rocket. The present SPID was designed to maximize the airflow through the detector. It should be considered whether a reduced airflow through the probe can be achieved so that ions do not enter the instrument while at the same time the MSPs still enter it.

Bibliography

Alcala, C., Kelley, M., and Ulwick, J. (2001). Nonturbulent layers in polar summer mesosphere: 1. detection of sharp gradients using wavelet analysis. *Radio Science*, 36(5):875–890.

Antonsen, T. (2013). On the internal physical conditions in dust probes: transport, heating and evaporation of fragmented dust particles. Master's thesis, UiT Norges arktiske universitet.

Antonsen, T. (2019). *In-situ Measurements of Mesospheric Aerosols-On the observable characteristics of nanoscale ice and meteoric smoke particles*. PhD thesis, UiT Norges arktiske universitet.

Antonsen, T. and Havnes, O. (2015). On the detection of mesospheric meteoric smoke particles embedded in noctilucent cloud particles with rocket-borne dust probes. *Review of Scientific Instruments*, 86(3):033305.

Antonsen, T., Havnes, O., and Mann, I. (2017). Estimates of the size distribution of meteoric smoke particles from rocket-borne impact probes. *Journal of Geophysical Research: Atmospheres*, 122(22).

Antonsen, T., Havnes, O., and Spicher, A. (2019). Multi-scale measurements of mesospheric aerosols and electrons during the maxidusty campaign. *Atmospheric Measurement Techniques*, 12(4):2139–2153.

Asmus, H., Staszak, T., Strelnikov, B., Lübken, F.-J., Friedrich, M., and Rapp, M. (2017). Estimate of size distribution of charged msps measured in situ in winter during the wadis-2 sounding rocket campaign. In *Annales Geophysicae*, volume 35, pages 979–998. Copernicus GmbH.

Baines, M., Williams, I., Asebiomo, A., and Agacy, R. (1965). Resistance to the motion of a small sphere moving through a gas. *Monthly Notices of the Royal Astronomical Society*, 130(1):63–74.

Bardeen, C., Toon, O., Jensen, E., Marsh, D., and Harvey, V. (2008). Numer-

ical simulations of the three-dimensional distribution of meteoric dust in the mesosphere and upper stratosphere. *Journal of Geophysical Research: Atmospheres*, 113(D17).

Baumann, C., Rapp, M., Anttila, M., Kero, A., and Verronen, P. T. (2015). Effects of meteoric smoke particles on the d region ion chemistry. *Journal of Geophysical Research: Space Physics*, 120(12):10–823.

Becker, E. and Schmitz, G. (2002). Energy deposition and turbulent dissipation owing to gravity waves in the mesosphere. *Journal of the atmospheric sciences*, 59(1):54–68.

Belova, E., Kirkwood, S., Ekeberg, J., Osepian, A., Häggström, I., Nilsson, H., and Rietveld, M. (2005). The dynamical background of polar mesosphere winter echoes from simultaneous eiscat and esrad observations. *Annales Geophysicae*, 23(4):1239–1247.

Belyaev, A. N. (2019). Local temperature changes in the mesosphere due to a "horizontally propagating" turbulent patch. *Journal of Atmospheric and Solar-Terrestrial Physics*.

Bird, G. (2005). The ds2v/3v program suite for dsmc calculations. In *AIP conference proceedings*, volume 762, pages 541–546. AIP.

Bittencourt, J. A. (2013). *Fundamentals of plasma physics*. Springer Science & Business Media.

Brattli, A., Blix, T., Lie-Svendsen, Ø., Hoppe, U.-P., Lübken, F.-J., Rapp, M., Singer, W., Latteck, R., and Friedrich, M. (2006). Rocket measurements of positive ions during polar mesosphere winter echo conditions. *Atmospheric chemistry and physics*, 6(12):5515–5524.

Brekke, A. (2013). *Physics of the upper polar atmosphere*. Springer Science & Business Media, Berlin, 2 edition.

CCMS, C. C. M. c. (2019). MSIS-E-90 atmosphere model.

Chen, F. F. (1984). *Introduction to plasma physics and controlled fusion*, volume 1:Plasma physics. Springer, New York, 2 edition.

Chun-Lin, L. (2010). A tutorial of the wavelet transform. *NTUEE, Taiwan*.

Cooley, J. W., Lewis, P. A., and Welch, P. D. (1969). The fast fourier transform and its applications. *IEEE Transactions on Education*, 12(1):27–34.

Darian, D., Marholm, S., Paulsson, J. J. P., Miyake, Y., Usui, H., Mortensen, M., and Miloch, W. J. (2017). Numerical simulations of a sounding rocket in ionospheric plasma: Effects of magnetic field on the wake formation and rocket potential. *Journal of Geophysical Research: Space Physics*, 122(9):9603–9621.

Doviak, R. J. et al. (1993). *Doppler radar and weather observations*. Elsevier, Amsterdam, 2 edition.

Farris, M. and Russell, C. (1994). Determining the standoff distance of the bow shock: Mach number dependence and use of models. *Journal of Geophysical Research: Space Physics*, 99(A9):17681–17689.

Folkestad, K., Hagfors, T., and Westerlund, S. (1983). Eiscat: An updated description of technical characteristics and operational capabilities. *Radio Science*, 18(6):867–879.

Havnes, O. and Kassa, M. (2009). On the sizes and observable effects of dust particles in polar mesospheric winter echoes. *Journal of Geophysical Research: Atmospheres*, 114(D9).

Havnes, O., Latteck, R., Hartquist, T., and Antonsen, T. (2018). First simultaneous rocket and radar detections of rare low summer mesospheric clouds. *Geophysical Research Letters*, 45(11):5727–5734.

Havnes, O. and Næsheim, L. I. (2007). On the secondary charging effects and structure of mesospheric dust particles impacting on rocket probes. *Annales Geophysicae*, 25:623—-637.

Havnes, O., Trøim, J., Blix, T., Mortensen, W., Næsheim, L., Thrane, E., and Tønnesen, T. (1996). First detection of charged dust particles in the earth's mesosphere. *Journal of Geophysical Research: Space Physics*, 101(A5):10839–10847.

Hedin, J., Gumbel, J., and Rapp, M. (2007). On the efficiency of rocket-borne particle detection in the mesosphere. *Atmospheric Chemistry and Physics*, 7(14):3701–3711.

Heisenberg, W. (1948). On the theory of statistical and isotropic turbulence. *Proceedings of the Royal Society of London. Series A. Mathematical and Physical Sciences*, 195(1042):402–406.

Hervig, M. E., Deaver, L. E., Bardeen, C. G., Russell III, J. M., Bailey, S. M., and Gordley, L. L. (2012). The content and composition of meteoric smoke in

mesospheric ice particles from sofie observations. *Journal of Atmospheric and Solar-Terrestrial Physics*, 84:1–6.

Horányi, M., Gumbel, J., Witt, G., and Robertson, S. (1999). Simulation of rocket-borne particle measurements in the mesosphere. *Geophysical Research Letters*, 26(11):1537–1540.

Hunten, D. M., Turco, R. P., and Toon, O. B. (1980). Smoke and dust particles of meteoric origin in the mesosphere and stratosphere. *Journal of the Atmospheric Sciences*, 37(6):1342–1357.

Kirkwood, S., Chilson, P., Belova, E., Dalin, P., Häggström, I., Rietveld, M., and Singer, W. (2006). Infrasound - the cause of strong polar mesosphere winter echoes? *Annales Geophysicae*, 24(2):475–491.

Kolmogorov, A. N. (1941). Dissipation of energy in locally isotropic turbulence. In *Akademiia Nauk SSSR Doklady*, volume 32, page 16.

Kurihara, J., Oyama, K.-I., Iwagami, N., and Takahashi, T. (2006). Numerical simulation of 3-d flow around sounding rocket in the lower thermosphere. In *Annales Geophysicae*, volume 24, pages 89–95.

Latteck, R., Singer, W., Rapp, M., and Renkwitz, T. (2010). Maarsy â€" the new mst radar on andÃ¸ya/norway. *Advances in Radio Science*, 8:219–224.

Latteck, R. and Strelnikova, I. (2015). Extended observations of polar mesosphere winter echoes over andøya (69° n) using maarsy. *Journal of Geophysical Research: Atmospheres*, 120(16):8216–8226.

Lübken, F.-J., Hillert, W., Lehmacher, G., and Von Zahn, U. (1993). Experiments revealing small impact of turbulence on the energy budget of the mesosphere and lower thermosphere. *Journal of Geophysical Research: Atmospheres*, 98(D11):20369–20384.

Mann, I. (2009). In *Meteors,in: (J. Trümper, Ed.) Landolt-Börnstein New Series*, pages 563–581. Springer, New York.

Megner, L. (2008). *Meteoric aerosols in the middle atmosphere.* PhD thesis, Meteorologiska institutionen (MISU).

Megner, L., Rapp, M., and Gumbel, J. (2006). Distribution of meteoric smoke–sensitivity to microphysical properties and atmospheric conditions. *Atmospheric Chemistry and Physics*, 6(12):4415–4426.

Meyers, S. D., Kelly, B. G., and O'Brien, J. J. (1993). An introduction to wavelet analysis in oceanography and meteorology: With application to the dispersion of yanai waves. *Monthly weather review*, 121(10):2858–2866.

Miloch, W. J. (2010). Wake effects and mach cones behind objects. *Plasma Physics and Controlled Fusion*, 52(12):124004.

Pineau, A. (2017). Optimizing the conditions in a dust probe for mesospheric rocket experiments. Technical report, Université Paris-Sud and University of Tromsø.

Plane, J. M., Feng, W., and Dawkins, E. C. (2015). The mesosphere and metals: Chemistry and changes. *Chemical reviews*, 115(10):4497–4541.

Rapp, M. and Lübken, F.-J. (2004). Polar mesosphere summer echoes (pmse): Review of observations and current understanding. *Atmospheric Chemistry and Physics*, 4(11/12):2601–2633.

Rapp, M., Lübken, F.-J., and Blix, T. (2003). Small scale density variations of electrons and charged particles in the vicinity of polar mesosphere summer echoes. *Atmospheric Chemistry and Physics*, 3(5):1399–1407.

Robertson, S., Dickson, S., Horányi, M., Sternovsky, Z., Friedrich, M., Janches, D., Megner, L., and Williams, B. (2014). Detection of meteoric smoke particles in the mesosphere by a rocket-borne mass spectrometer. *Journal of atmospheric and solar-terrestrial physics*, 118:161–179.

Rosinski, J. and Snow, R. (1961). Secondary particulate matter from meteor vapors. *Journal of Meteorology*, 18(6):736–745.

Sagalyn, R. C., Smiddy, M., and Wisnia, J. (1963). Measurement and interpretation of ion density distributions in the daytime f region. *Journal of Geophysical Research*, 68(1):199–211.

Saunders, R. W. and Plane, J. M. (2006). A laboratory study of meteor smoke analogues: Composition, optical properties and growth kinetics. *Journal of Atmospheric and Solar-Terrestrial Physics*, 68(18):2182–2202.

Schunk, R. and Nagy, A. (2009). *Ionospheres: physics, plasma physics, and chemistry*. Cambridge university press.

Seppälä, A., Clilverd, M., Rodger, C., Verronen, P., and Turunen, E. (2008). The effects of hard-spectra solar proton events on the middle atmosphere. *Journal of Geophysical Research: Space Physics*, 113(A11).

Smiley, B., Rapp, M., Blix, T., Robertson, S., Horányi, M., and Latteck, R. (2003). Measuring the charge and size distribution of charged aerosol particles inside pmse and nlc. In *European Rocket and Balloon Programmes and Related Research*, volume ESA-SP 530, pages 537–542.

Smirnov, R., Pigarov, A. Y., Rosenberg, M., Krasheninnikov, S., and Mendis, D. (2007). Modelling of dynamics and transport of carbon dust particles in tokamaks. *Plasma Physics and Controlled Fusion*, 49(4):347.

Sounding Rockets Program Office (2015). Nasa sounding rockets user handbook. Technical report.

Spicher, A., Miloch, W., and Moen, J. (2014). Direct evidence of double-slope power spectra in the high-latitude ionospheric plasma. *Geophysical Research Letters*, 41(5):1406–1412.

Strelnikov, B., Rapp, M., and Lübken, F.-J. (2003). A new technique for the analysis of neutral air density fluctuations measured in situ in the middle atmosphere. *Geophysical Research letters*, 30(20).

Surdal, L., Havnes, O., and Philbrick, C. (2009). Mesospheric dust and its secondary effects as observed by the esprit payload. *Annales Geophysicae*, 27:1119–1128.

Torrence, C. and Compo, G. P. (1998). A practical guide to wavelet analysis. *Bulletin of the American Meteorological society*, 79(1):61–78.

Vallis, G. K. (2017). *Atmospheric and oceanic fluid dynamics*. Cambridge University Press, 2 edition.

Yau, A. W., Whalen, B. A., and McEwen, D. (1981). Rocket-borne measurements of particle pulsation in pulsating aurora. *Journal of Geophysical Research: Space Physics*, 86(A7):5673–5681.

Yunus, A. C. (2014). *Fluid Mechanics: Fundamentals And Applications (Si Units)*. Tata McGraw Hill Education Private Limited, Sigapore, 3rd, si units edition.
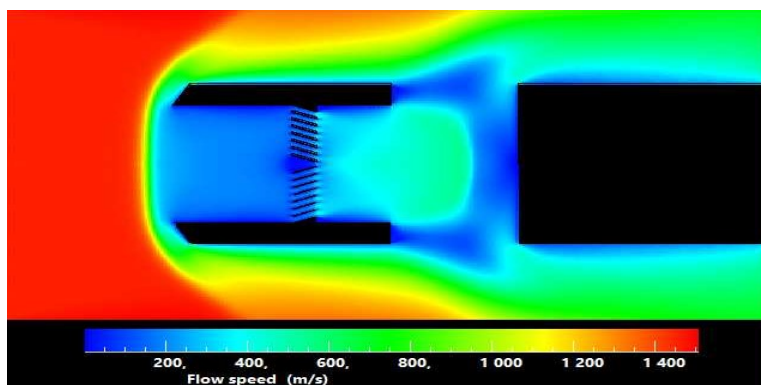
Appendix
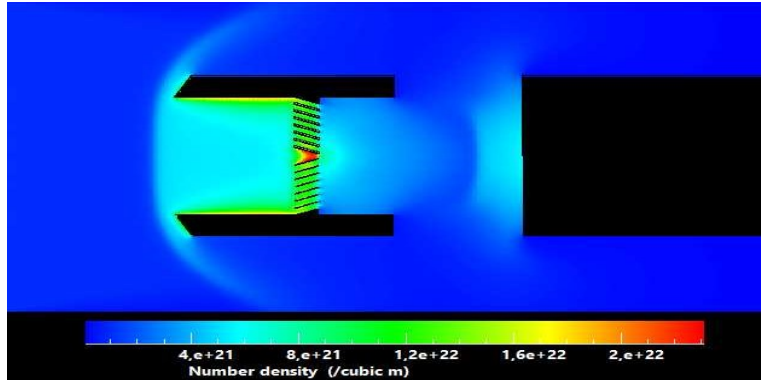
(a)
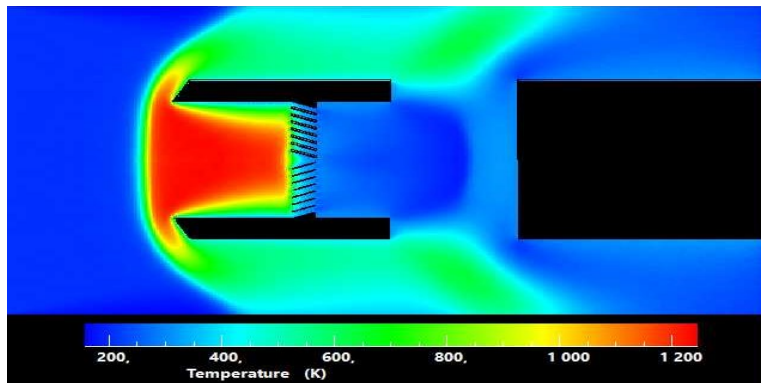
(b)

(c)

Figure 1: Results from DSMC for 85 km for neutral gas flow. (a) Number density per cubic meter. (b) Temperature in Kelvin. (c)Speed in meters per second